DEUTSCHES ELEKTRONEN-SYNCHROTRON
Ein Forschungszentrum der Helmholtz-Gemeinschaft

DESY 21-233
December 2021

Vacancy-Dynamics in Niobium and its Native Oxides and Their Potential Implications for Quantum Computing and Superconducting Accelerators

M. Wenskat et al.

ISSN 0418-9833

NOTKESTRASSE 85 - 22607 HAMBURG

Herausgeber und Vertrieb:

Verlag Deutsches Elektronen-Synchrotron DESY

DESY Bibliothek
Notkestr. 85
22607 Hamburg
Germany

Vacancy-Dynamics in Niobium and its Native Oxides and their potential implications for Quantum Computing and Superconducting Accelerators

Marc Wenskat,[1,*] Jakub Čižek,[2] Maciej Oskar Liedke,[3] Maik Butterling,[3] Martin Stiehl,[4] Guilherme Dalla Lana Semione,[1,5,6] Constanze Backes,[4] Christopher Bate,[1,5] Oksana Melikhova,[2] Eric Hirschmann,[3] Andreas Wagner,[3] Hans Weise,[5] Andreas Stierle,[5] Martin Aeschlimann,[4] and Wolfgang Hillert[1]

[1] *Institute of Experimental Physics, University of Hamburg, Germany*
[2] *Faculty of Mathematics and Physics, Charles University, Czech Republic*
[3] *Institute of Radiation Physics, Helmholtz-Zentrum Dresden-Rossendorf, Germany*
[4] *Department of Physics, Technical University of Kaiserslautern, Germany*
[5] *Deutsches Elektronen-Synchrotron DESY, Germany*
[6] *MAPEX Center for Materials and Processes, University of Bremen, Germany*

(Dated: October 5, 2022)

In recent years, superconducting radio-frequency (SRF) cavities have been considered as candidates for qubits in quantum computing, showing longer photon lifetimes and, therefore, longer decoherence times of a cavity stored qubit compared to many other realizations. In modern particle accelerators, SRF cavities are the workhorse. Continuous research and development efforts are being undertaken to improve their properties, to increase the accelerating field and lower the surface resistance, which in turn increase the energy reach and duty cycle of accelerators. While some experimental milestones have been achieved, the mechanisms behind the still observed losses remain not fully understood. In this contribution we are going to show that a recently reported temperature treatment of Nb SRF cavities in the temperature range of 573-673 K, which reduces the residual surface resistance to unprecedented values, is linked to a reorganization of the niobium oxide and near-surface vacancy structure and that this reorganization can explain the observed improved performance in both applications, quantum computing and SRF cavities.

Keywords: Superconductor, Vacancies, Oxide, DFT, Quantum Computing

I. INTRODUCTION

Electrical properties of oxides are significantly affected by vacancy-like defects. For instance, it is known that oxygen vacancies can lead to an n-type doping, which causes surface magnetism of otherwise dielectric material [1–3]. Such local *magnetic impurities* have already caught the attention of the superconducting radio-frequency (SRF) community. They can cause subgap states, which alter the performance of SRF cavities by contributing to dissipation mechanisms [4–9].
Whenever SQUIDs were used as qubits or, in modern architecture of qubits, the so-called Transmon, the oxide layer act as weak link and contains many defects. These defects are described as lossy two-level systems (TLS), which severely limit the coherence time to just a few nanoseconds, [10–15]. To increase the coherence time is the major goal in developing technical realizations of qubits, hence a better understanding of microscopic realizations of TLS is mandatory. And in fact, oxygen-vacancies have been suggested as ideal candidates for TLS [16–18]. For example, in [17], the surface vacancy states of Al_2O_3 and SiO_2 were studied using density functional theory (DFT), resulting in dangling bond states on the surface assembling localized magnetic moments. Such dangling bonds are exemplary realizations for a TLS in an amorphous material, and can increase the noise level [19]. Another example are hydrogen-vacancy complexes which can act as TLS, as they form the so-called threefold degenerate rotors with tunnel splittings in the MHz to GHz range [16]. In particular, hydrogen-vacancy complexes in niobium have been proven to exist and are considered to have detrimental impact onto the RF performance. All those different realizations of TLS can provide a microscopic explanation of the observations in the recent application of SRF cavities for quantum computing [20, 21], in which photon lifetimes of 2 s were observed, after the niobium surface underwent a dedicated annealing procedure.
This procedure, namely an annealing treatment at 573-673 K *in-situ* for 3 h in UHV (the newly dubbed "Mid-T Bake"), showed extremely high quality factors of $Q_0 \approx 5 \times 10^{10}$ with a residual resistance below 1 nΩ at 2 K [22]. In addition, a behavior called "anti-Q-slope", which is a positive slope of the Q_0 as a function of the accelerating field E_{acc} was observed. This implies a reduction of the resistance, as described by the BCS theory, with increasing accelerating field. Such behavior has been observed for 1.3 GHz only in the case of so-called *doped* cavities so far [23, 24] and is not well understood yet, although theoretical treatments do predict the counter-intuitive phenomenon [25, 26]. There are reports of anti-Q-slope behavior on 3.9 GHz cavities [24] and 3 GHz cavities [27], both without doping. This frequency dependence might help to identify the microscopic origin of this behavior [9, 28, 29, 66]. As has been reported by He et al. and Ito et al. [30, 31], the Mid-T Bake was

* marc.wenskat@desy.de

successfully reproduced at other labs rather fast. Moreover, the requirements on the process parameters have been further relaxed, i.e. using standard furnaces and simplified handling with niobium caps installed on cavities, rather than *in-situ* annealing of whole cavities and their transport while still under vacuum to the cryogenic RF testing area, as been done by Posen et al.[22].

The aim of this work is twofold: (i) to study vacancies in the native niobium oxide, as potential cause for the reduced coherence time but also as cause for sub-gap states, increasing the surface resistance of cavities. (ii) to study vacancy-complexes within the niobium, which influences the interstitial oxygen and hydrogen concentration and therefore plays an important role in the formation of *nanohydrides*, also increasing the surface resistance of cavities.

In order to investigate the vacancy dynamics, we utilized positron spectroscopy. As positrons can easily get trapped in metal vacancy defects and are known to be very sensitive to their elemental environment, they are the optimal choice to analyze the types, concentrations, and atomic environment of empty crystal sites [36]. Hence, we looked with *in-situ* and *ex-situ* experiments at the dynamics. To analyze and interpret the obtained data, we used *ab-initio* calculations. Complementary to these methods, we applied X-ray reflectivity (XRR), which is a widely-employed technique to study thin films and multi-layered materials, to observe the niobium-oxide development and dissolution during the annealing procedures. This was crucial for the further discussion, as those layers act as primary source for interstitial diffusion of oxygen and has a significant influence on the material structure in the near-surface region. Guided by our results and theoretical models, we started to study the magnetic order of the oxide. For this we identified Kerr microscopy as the most versatile method and proofed the existence of magnetic domains in the niobium oxide.

In this work we report on the vacancy dynamics and their interactions with oxygen and hydrogen as interstitials in niobium, by applying various annealing temperatures, as well as the kinematics in the native oxide layer. Furthermore, how the same microscopic states (oxygen defects and interstitial trapping at vacancies) can explain the observations in SRF cavities for different applications - namely quantum computing and accelerators.

II. METHODS

A. X-ray reflectivity

In the frame of this work Nb(100) specimen were studied after step-wise sequential annealing under UHV vacuum conditions. Each step was followed by *in-situ* XRR measurements using a photon energy of 70 keV. Data were collected using a Maxipic 2D, used for sample alignment and to perform XRR measurements [34]. A formalism developed in [32] takes effects of multiple scattering events and interfaces into account. The XRR curves were fitted using the Parrat formalism with FEWLAY, taking into account finite resolution effects [33]. For each layer j of the fit model a set of four parameters was attributed by the fitting routine: layer thickness d_j, layer roughness σ_j and the optical quantities δ_j and β_j, which compose the index of refraction n_j of the probed layer [34].

B. Positron annihilation spectroscopy

In principle, two approaches can be utilized: (i) positron annihilation lifetime spectroscopy (PALS), where positron lifetime in a material is measured and (ii) Doppler broadening (DB) of the annihilation photo-peak, which is realized as a measurement of the Doppler shift of annihilation radiation [37]. The positron lifetime is governed by the local electron density at the positron annihilation site, i.e. PALS provides information about the type and concentration of open volume defects in a material [38]. The Doppler shift of the annihilation radiation is determined by the momentum of the electron, which annihilated the positron. In DB positron annihilation spectroscopy (PAS), the broadening of the annihilation photo-peak is characterized in terms of the line shape parameters S (sharpness) and W (wing), which contain information about the contributions of annihilation by low or high momentum electrons, respectively. Hence, the correlated measurement of S- and W-parameters is also sensitive to the type and the atomic environment of positron trapping sites or defects. More details on the method is given in the Appendix B

Depth resolved variable energy positron annihilation spectroscopy (VEPAS) studies of the sub-surface region were carried out at the Helmholtz Zentrum Dresden-Rossendorf on a continuous slow positron beam "SPONSOR" [39] with an apparatus for *in-situ* defect studies "AIDA" [40] employing DB-VEPAS, as well as on a pulsed positron beam "MePS" [41] at the ELBE facility employing positron lifetime (VEPALS). The spot size diameter of the positron beams was in the order of $5-6$ mm and the energy of incident positrons was adjusted the range 0.05-36 keV for DB-VEPAS (it corresponds to the mean positron penetration depth into Nb from 0.02 to 1380 nm) and 1-10 keV for VEPALS (it corresponds to the mean positron penetration depth into Nb from 4.7 to 394 nm). Both DB-VEPAS and VEPALS measurements were done *in-situ*, i.e. samples were baked in the sample chamber with simultaneous irradiation by the slow positron beam. The data obtained at MePS were analyzed using the PALSfit3 software [42] and the plots were generated using OriginLab [43].

C. Kerr microscopy

This microscopical approach utilizes the magneto-optical Kerr effect to visualize and characterize the magnetic behavior of materials and is a well established technique to study magnetization. The system used is an in-plane Kerr magnetometer (Zeiss Axio Imager Z2 Vario upgraded by Evico Magnetics GmbH) and a magnetic field in the range of ±200 mT was applied. The measurements were done at room temperature with sensitivity to the first 15 nm of the surface. The in-plane orientation of the magnetic field and the applied field values are similar to what the niobium surface experiences during accelerator operation. The small penetration depth is also beneficial to be more sensitive to oxide layer effects and of a similar order of magnitude of the London penetration depth of niobium, probing the surface relevant for the SRF behavior. On each sample, an area of $672 \times 554\,\text{pixels}^2$ or $\approx 448 \times 369\,\mu\text{m}^2$ was scanned to obtain the magnetization curve, while multiple, smaller areas were also scanned to study the spatial homogeneity of the hysteresis and investigate regions of interest.

D. *Ab-initio* calculations

Vacancies in Nb and their complexes with the most relevant gas impurities (H, O, N) were modeled using density functional theory (DFT) implemented in the Vienna *ab-initio* simulation package (VASP) [44, 45]. Electronic structure calculations were performed employing the projector augmented wave (PAW) method [46]. The generalized gradient approximation (GGA) with the exchange-correlation functional of Perdew–Burke–Ernzerhof (PBE) [47] was used. The calculations were performed using supercells containing 128 atomic sites and consisting of $4 \times 4 \times 4$ bcc unit cells with the lattice parameter $a = 3.322$ Å obtained by structure optimization. The energy cut-off of the plane wave basis of 500 eV and Fermi smearing of the electronic occupancy with a width of 0.2 eV were used in all calculations. Reciprocal space was sampled using $3\times3\times3$ k-point mesh generated applying the Monkhorst-Pack scheme [48]. Convergence tests revealed that calculated energies are converged to within ≈ 0.01 eV. Equilibrium geometries of defects were determined by fully relaxing ion positions and volume of the supercell. Structural relaxations were performed until forces on each atom were smaller than ≈ 0.01 eV/Å. Positron annihilation observables were calculated using DFT within the so-called standard scheme [49]. In this approximation, the positron density is assumed to be negligibly small everywhere and not affecting the bulk electron structure. The momentum distribution of the annihilating electron-positron pairs was calculated using the approach described in Refs. [50, 51]. Further background is given in the Appendix C.

E. Samples

The samples used for the positron studies and the Kerr microscopy were cut out of a niobium sheet from the European XFEL cavity production, where the sheet was produced by Tokyo Denkai Co. Ltd and the mechanical and chemical properties of the Nb sheets supplied by the producer are summarized in Table I.

TABLE I. Material properties of the niobium sheets: Vickers hardness (HV), tensile strength (R_m), yield strength (R_p), concentration of vacancies (c_v),concentration of oxygen (c_O), nitrogen (c_N), hydrogen (c_H) and carbon (c_C).

	Tokyo Denkai
HV	42.5-50.6
R_m[N/mm^2]	170
R_p[N/mm^2]	62
c_v[ppm at]	8-10
c_O[ppm at]	3.5-4.5
c_N[ppm at]	3.2-4.4
c_H[ppm at]	0.5-0.8
c_C[ppm at]	0.2-0.7

The sample geometry is of flat-conical design, with a base diameter of 12 mm, a top diameter of 10 mm and a thickness of 2.8 mm. They were cut from the sheet by a water jet cutter and turned to its final shape. The samples used for positron spectroscopy and Kerr microscopy were prepared following closely the standard cavity preparation and the intermediate cleaning and rinsing was carried out in an ISO 4 cleanroom environment [52–55], see Appendix A for details.
The samples used for the X-ray reflectivity measurements were mechanically polished single-crystal niobium (100) samples of cylindrical design (10 mm diameter, 2 mm height) oriented to better than 0.1°. The samples were annealed at 2273 K for 6 h by induction heating in an ultrahigh vacuum (UHV) at a starting pressure of 10^{-10} mbar and unavoidably exposed to air for several days before the experiments. This procedure ensures that the Nb single crystals are as clean as possible in the bulk.

III. RESULTS

A. *In-situ* X-ray reflectivity

With the exception of measurements at room temperature, *in-situ* XRR curves were collected twice for each temperature step: first, after the sample temperature was deemed stable following an increase in the heater current (usually 1 hour, here labeled t_1) and a second time after more than 12 hours of annealing (labeled t_2). All collected and fitted XRR curves together with the respective electron density profiles are shown in Fig. 1.
At first, as shown in Fig. 1, the natural oxide layer presented the typical composition from the surface to the

metal/oxide interface with Nb_2O_5, NbO_2 and NbO displaying layer thicknesses of 1.8, 1.3 and 0.8 nm (error bar of ±0.1 nm) with associated roughness between 0.2 and 0.4 nm for the oxide/metal interfaces[34]. The same stack order is observed upon annealing at 393 K for both times t_1 and t_2. Initially (time t_1), the oxides are virtually non-affected by the annealing treatment, with their respective thicknesses and roughness values remaining within the uncertainty of the fits (±0.1 nm). Hardly affecting Nb_2O_5 and NbO, the extended annealing at 393 K (time t_2) leads to a partial consumption of NbO_2, as observed by a decrease of 0.2 nm in its layer thickness. Meanwhile, all roughness values remained in a similar range.

At 473 K a pronounced reduction of the oxide thickness was observed. After ≈ 1 hour (t_1), the thickness of the outer-most oxides, Nb_2O_5 and NbO_2, decreased to 0.6 and 0.3 nm, respectively. By contrast, the NbO layer thickness increased to 1.1 nm. Nevertheless, the total oxide thickness at this stage decreases to about 2 nm, which corresponds to a drop of ≈ 54%. Further annealing at 473 K (time t_2) only affected the roughness of the NbO/Nb interface, which raised by 0.25 nm.

The complete consumption of Nb_2O_5 was achieved at 523 K after ≈1 hour (t_1) already. At this stage NbO_2 was also partially removed, reaching a layer thickness of 0.8 nm. As the annealing time at 523 K is extended (time t_2), a progressive etching of NbO_2 to 0.7 nm was indicated by the analysis, although the difference between the thicknesses obtained from the curves t_1 and t_2 falls within the error bar of the fits.

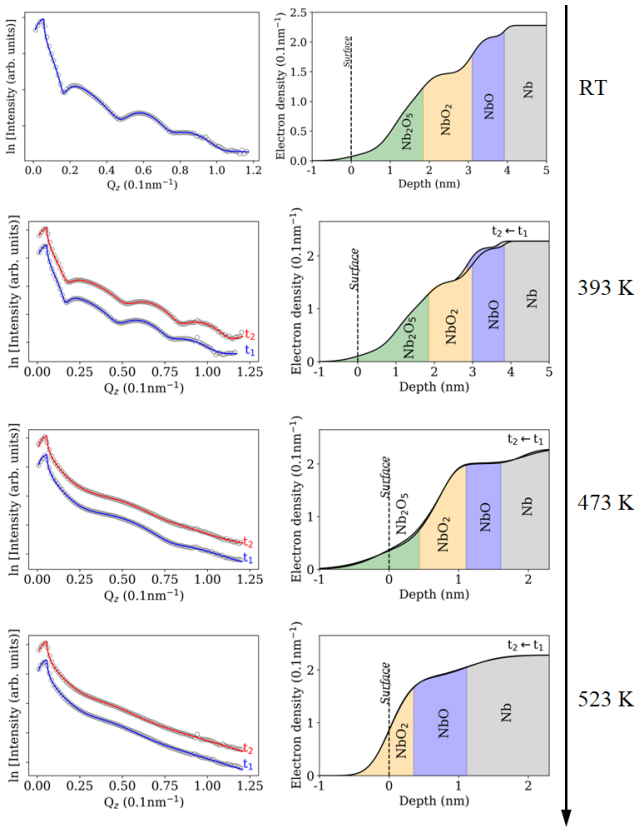

FIG. 1. Left: X-ray reflectivity data (open circles) measured with photon energies of 70 keV with the respective fits (solid lines). The scans are offset in y-direction. Right: Electron-density profiles obtained from the fits of the data. The measurement collected data from RT up to 523 K.

B. *In-situ* Doppler broadening variable energy positron annihilation spectroscopy (DB-VEPAS)

The *in-situ* annealing of a Nb sample has been conducted in the AIDA chamber [40] with simultaneous DB-PAS measurements at constant E_p=1.5 keV. The annealing scheme is sketched in Fig. 2 a). A constant ramping rate of 1 K/min was used and each up ramp was followed by a 4 h dwell at the target temperature in the absolute range of 343 − 573 K and a subsequent ramping down to room temperature (RT). The data were continuously collected and accumulated as 600 s packages. The annihilation line parameters S and W, as well as the $3\gamma/2\gamma$ ratio, were calculated from the data and are presented as a function of the overall experiment time in Fig. 2 b), c), and d), respectively. After each ramp down to RT, a full positron implantation energy E_p (depth) scan was conducted in order to estimate defect microstructure steady states. The measured $S(E_p)$ curves are plotted in Fig. 3, while Fig. 4 shows the S-W plot for positron energy E_p=1.5 keV corresponding to the mean positron penetration depth of about 9 nm. For all samples, the observable changes take place in a range of about ≈ 170 nm (see Fig. 3). This is sufficient to dominate the RF performance, since the effective London penetration depth λ_L at 2 K is about 39 nm for pure niobium and up to 200 nm for niobium in the Pippard-limit, which refers to a niobium with an interstitial concentration resulting in a mean-free path ℓ smaller than the coherence length ξ_0 [57]. No significant changes were observed during baking up to 353 K. Only annealing at temperatures above 353 K has a significant influence. All samples showed an steady increase (decrease) of the S (W) parameter during the baking for 4 h up to 473 K, respectively (Figs. 2 and 4). In the S(time) and W(time) curves the influence of ramping up and down is evident but the final values at the respective temperature stages are larger (smaller) than the preceding steps. Moreover, during the 4 h dwell time a kinematic evolution of S and W is noticeable, evidencing a raise in open volume. For larger temperatures an opposite trend dominates and S (W) parameters non-monotonically decrease (increase), which is a fingerprint of defect density drop and a change of its type. All S-W values are on the same line up to 473 K (Fig. 4). However, annealing at 523 K resulted in a change of slope in the S-W plot and a shift to higher W values indicating a change in the nature of positron annihilation sites. This change coincides with the dissolution of the Nb_2O_5 layer as seen with XRR, see Fig.1. Further annealing to 573 K

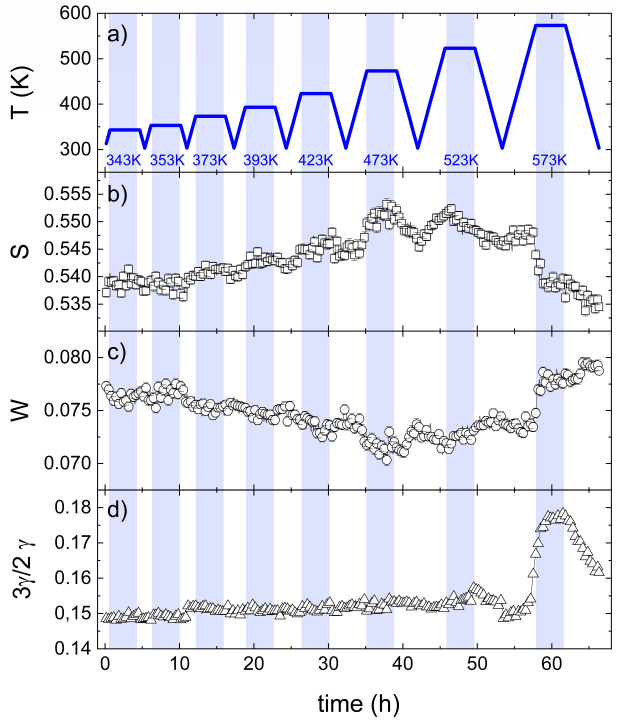

FIG. 2. *In-situ* annealing of a Nb sample in the AIDA chamber with simultaneous DB-PAS measurement at E_p=1.5 keV. A sketch of temperature variations during the experiment (a), where a constant ramping of 1 K/min was used followed by a 4 h dwell at a given temperature in the range of 343 − 573 K and ramping down to room temperature. Each measurement point represent 600 s of data acquisition. The annihilation line parameters: low electron momentum fraction S (b), high electron momentum fraction W (c), and $3\gamma/2\gamma$ ratio (d) as a function of the experiment time. Annealing dwell times are marked by the blue regions.

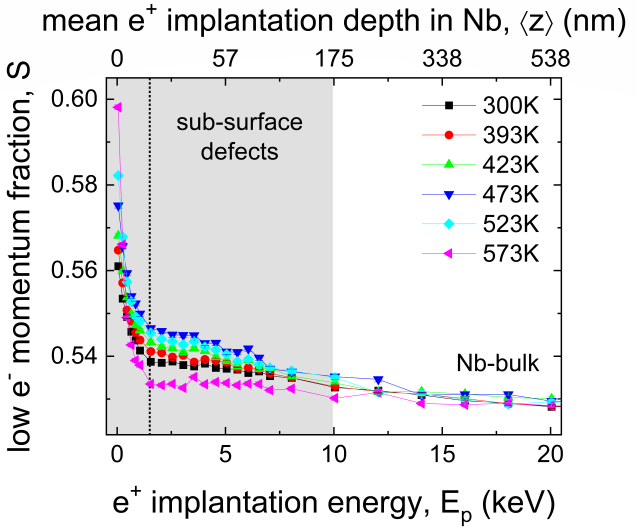

FIG. 3. Annihilation line parameter S as a function of positron implantation energy E_p and mean positron implantation depth $<z>$ after sequential *in-situ* annealing in the temperature range of T=300-573 K. The sub-surface region containing defects is marked in gray. A vertical line at E_p=1.5 keV denotes the depth selected for continuous DB-VEPAS measurements.

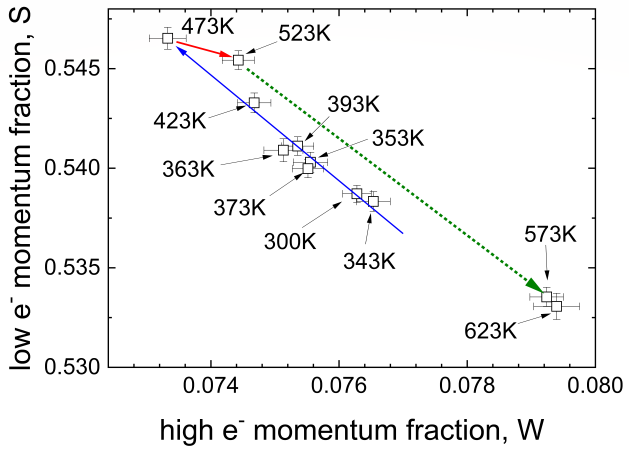

FIG. 4. S-W plane at a fixed energy (E_p=1.5 keV) of incident positrons. The arrows guide the eye and follow the temperature development. Three distinct slopes, and hence vacancy-impurity-complexes, are identified.

resulted in additional increase of W accompanied by a decrease of S. This change remains after cooling down to room temperature and further exposure to air, as shown in Fig. 5. It testifies to the formation of a new stable defect-type compared to the status before the annealing.

In Fig. 3 all depth profiles acquired at the RT intervals in between of the successive annealing stages are highlighted. For E_p < 2 keV a fast S decrease is observed which originates from the surface oxide states. In the range of 8< E_p <2 keV a step like plateau region is visible, which steadily decreases in magnitude to the Nb-bulk state for larger E_p. For temperatures up to 473 K the step becomes more convex turning afterwards to a more flat level closer to the Nb-bulk value of S at 573 K. The change of S between 523 K and 573 K is noticeably more abrupt than for preceding temperatures, as nicely presented in Fig. 4, too. Finally, the $3\gamma/2\gamma$ ratio for the positron energy E_p=1.5 keV is shown in Fig. 2. Up to 473 K only a small linear drift can be seen, which is due to surface cleaning effects. At 523 K an increase of $3\gamma/2\gamma$ ratio is observed, which can be explained as thermally activated release of positrons trapped in the surface image potential. This is further supported by the fact that $3\gamma/2\gamma$ ratio returns to its initial value before the anneal when the sample is *in-situ* cooled down to room temperature. At 573 K a significant increase of $3\gamma/2\gamma$ ratio was detected. After the heating period when the sample was cooled down to room temperature, $3\gamma/2\gamma$ ratio decreased again but still remained higher compared to the value before annealing. Similarly to what occurs in the annealing

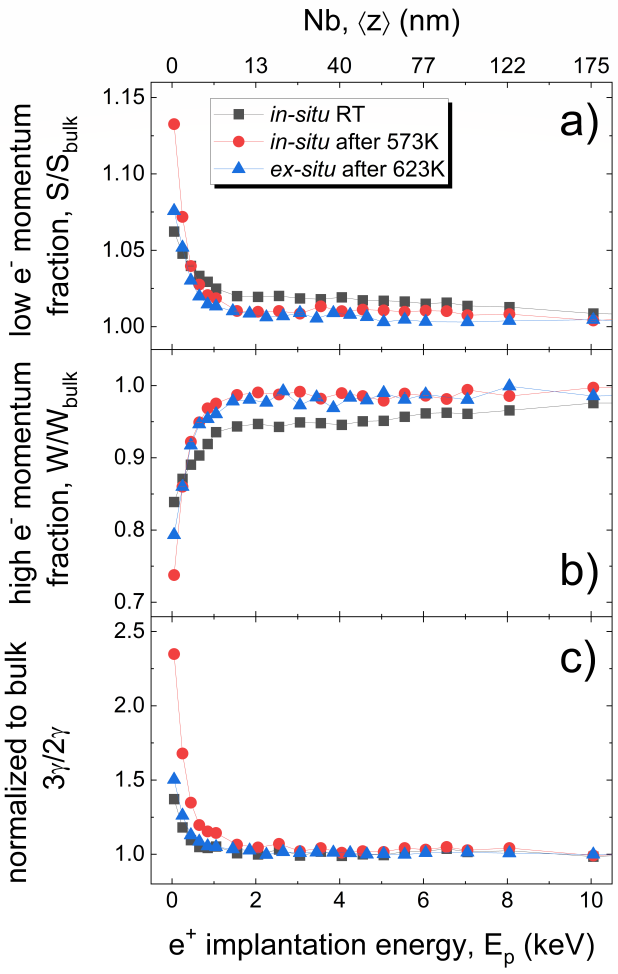

FIG. 5. Normalized to the bulk value annihilation line parameters S and W, as well as the $3\gamma/2\gamma$ ratio, as a function of the incident positron energy E_p. The curves show the *in-situ* AIDA measurement at room temperature (RT) before annealing (black), after annealing at 573 K measured still *in-situ* at RT (red), and the "*ex-situ*" measurement at RT after annealing at 623 K and subsequent exposure to air (blue).

at 523 K, thermally activated release of positrons trapped at surface potential well occurs also during annealing at 573 K. But the remaining increased $3\gamma/2\gamma$ ratio in the sample cooled down to room temperature showed that in addition to the release process a real change in the chemistry of the near-surface region occurred. This is further confirmed by the fact that even after the sample was exposed to air and remeasured, the $3\gamma/2\gamma$ ratio in the sub-surface region with depth of $\langle z\rangle \approx 9\,\text{nm}$ ($\langle z\rangle$ at E_p=1.5 keV) stayed above the value determined before the initial annealing, as shown in Fig. 5 c.

C. *In-situ* variable energy positron annihilation lifetime spectroscopy (VEPALS)

In order to better compare with the *in-situ* DB-PAS (2) and discuss the data, *in-situ* PALS measurements for positron energies of $E_p = 2\,\text{keV}$ (penetration depth ≈ 14 nm) and $E_p = 6\,\text{keV}$ (penetration depth ≈ 82 nm; not affected by surface effects) are presented simultaneously. For the discussion, the results for all temperatures are shown in one plot. The effects of temperature and annealing time are visible. Parameters of each component (lifetime and intensity) are discussed individually, and the overall result is shown in Fig. 6.

The reduced bulk lifetime τ_1 represents positron annihilation at interstitial crystal positions and stays almost constant at around 40 ps for the surface near region (E_p = 2 keV) and at about 70 ps for a deeper region (E_p = 6 keV). The intensity I_1 is almost constant for T < 473 K, and slightly decreases for T > 473 K, for both close to the surface and deeper in the sample. In case of E_p = 2 keV, the intensity I_1 slightly increases at the beginning of each annealing sequence (besides 523 K). This might be related to surface cleaning effects since it was not observed at larger implantation depths (6 keV). On the other hand, the fluctuations at 2 keV are mainly due to the short lifetime values, which are close to the detector resolution limit. For that reason, a more detailed discussion of the lifetime τ_1 for $E_p = 2\,\text{keV}$ is difficult.
The second component with lifetime τ_2 stays almost constant at around 150 ps for T < 393 K, indicating that Nb contains vacancies decorated by multiple hydrogen atoms (as shown in [56]). For annealing temperatures larger than 393 K the lifetime almost monotonically increases towards the value for a bare Nb vacancy revealing gradual release of hydrogen atoms from their complex with the vacancy. This behavior is similar for the surface-near region ($E_p = 2\,\text{keV}$) and the deeper region ($E_p = 6\,\text{keV}$). The intensity I_2 (which is a measure of vacancy concentration) shows a similar behavior: it remains constant up to 393 K and decreases for larger temperatures. It indicates that hydrogen removal is accompanied with annealing of single vacancies. However, at 523 K I_2 slightly increases indicating an onset of different physical process since hydrogen has been removed already.
The third component with lifetime τ_3 represents a contribution of positrons annihilated on the surface and positrons trapped at larger point defects (vacancy agglomerations). The lifetime τ_3 is almost constant for T < 393 K and increases for larger temperatures. As discussed in Ref. [56], this can only be explained by hydrogen release from vacancy-clusters (analog to the lifetime behavior of the decorated vacancies). At 523 K the lifetime τ_3 decreases for a positron energy of $E_p = 2\,\text{keV}$ (also very little for $E_p = 6\,\text{keV}$), again indicating an onset of a different physical process, that is more pronounced in the near surface region. The intensity I_3 increases for T > 353 K. Considering the behavior of intensity I_2 (simultaneous decrease), it can be explained by an overall

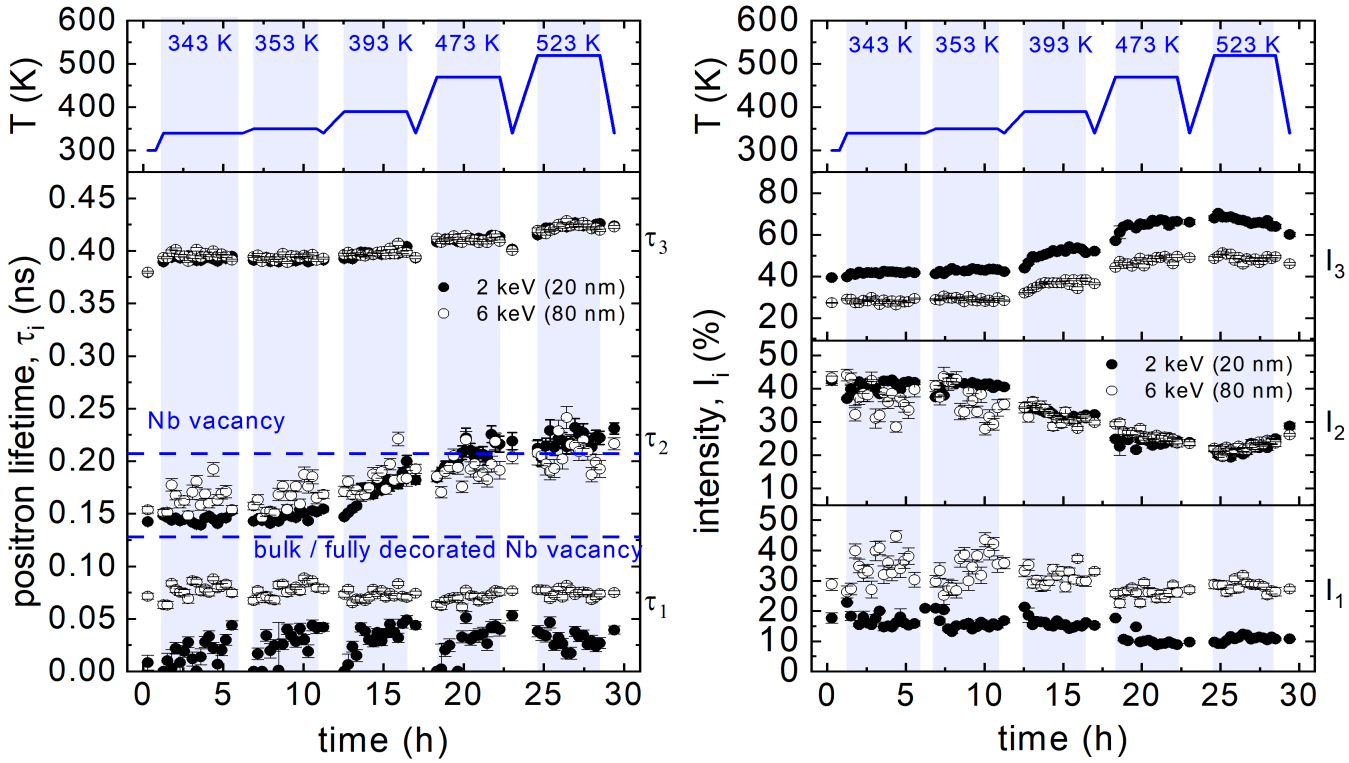

FIG. 6. Positron lifetimes τ_i (left) and corresponding intensities I_i (right) of components resolved in positron lifetime spectra plotted as a function of the measurement time for $E_p = 2\,\mathrm{keV}$ (closed circles) and $E_p = 6\,\mathrm{keV}$ (open circles). A sketch of temperature variations during the experiment is shown in the top layer of both figures and the blue areas indicate the temperature sequences.

decrease of the concentration of vacancy-type defects (Nb vacancy) and simultaneous increase in the concentration of vacancy clusters, i.e. after detachment of hydrogen vacancies agglomerate into clusters. The vacancy agglomerations are mostly expected in the oxide layers at the surface nearest region as suggested by the XRR (Fig. 1) and DB-VEPAS measurements (Fig. 3).

D. Kerr microscopy

Surface magnetic order can be observed in dielectric oxides and it is assumed that this is due to oxygen vacancies [1–3]. Hence, we studied the magnetic order of several samples within the first 15 nm at room temperature using Kerr microscopy as complimentary method to the positron spectroscopy. The magnetic field was applied parallel to the surface, which is the case under operation conditions of a superconducting cavity. Fig. 7 shows a single image taken with the Kerr microscope. The image displays a formation of a multi-domain structure ($d < 10\,\mu\mathrm{m}$) distributed across the sample surface, independent from grain boundaries. Furthermore, by scanning the focal plane of the microscope, the origin of this multi-domain structure was identified within the niobium oxide layer. This observation was found for all

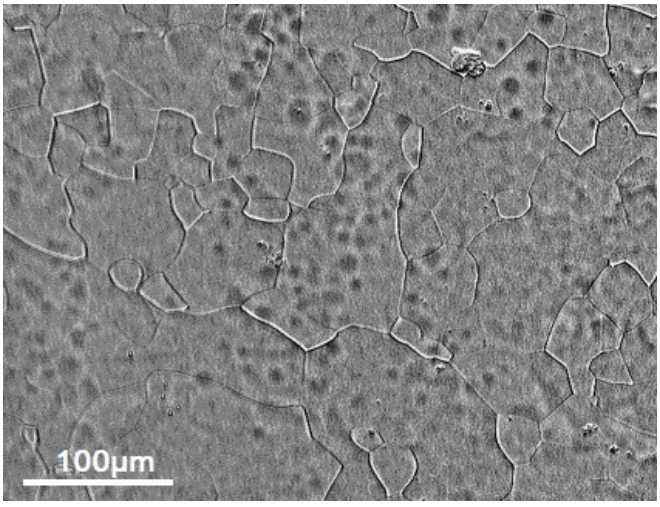

FIG. 7. Kerr image taken at 200 mT. Brighter areas are domains with a magnetization anti-parallel to dark areas. The grain boundary structure is clearly visible as continuous lines. A spotted multi-domain structure ($d < 10\,\mu\mathrm{m}$), overlaying the grain-boundaries and randomly distributed, is observed.

samples investigated.

E. *Ab-initio* calculations

In-detail calculations, leading to the results shown here are given in the Appendix. Calculated binding energies $E_{B,\text{v-X}}$ of H, N, O to a vacancy are summarized in Table II, indicating that oxygen is bound to a vacancy stronger than hydrogen. On the other hand, the binding of nitrogen to a vacancy is weaker compared to hydrogen. The calculated bond length, i.e. the distance of a gas atom from the vacancy $d_{\text{v-X}}$ is shown in Table II as well. Hydrogen is in the closest vicinity of a vacancy in contrast to the loosely bounded nitrogen located in a largest distance from the vacancy. The oxygen-vacancy distance is found between that for H and N. Complexes of vacancies

TABLE II. Calculated lifetimes τ of positrons trapped at vacancies and complexes of vacancies with H, N, O gas impurities. All these impurities are trapped at vacancies. Calculated binding energy $E_{B,\text{v-X}}$ of gas impurity X to vacancy and bond length d_{v-X}, i.e. distance of impurity X from vacancy, are listed in the table as well.

defect	τ (ps)	$E_{B,\text{v-X}}$ (eV)	$d_{\text{v-X}}$ (Å)
v	207	–	–
v-H	199	-0.57	1.43
v-N	190	-0.37	1.57
v-O	188	-0.83	1.53

with H, N, O impurities are capable of positron trapping. However, the lifetime of trapped positrons is shortened with respect to a bare vacancy due to a reduced positron localization and increased electron density in the vacancy. Calculated lifetimes of positrons trapped in v-H, v-N and v-O complexes are also listed in Table II. The shortening of the positron lifetime becomes more pronounced with an increasing number of protons Z of the impurity atom, i.e. the shortest lifetime was found for v-O complex.

Up to six hydrogen atoms can be trapped in a single vacancy, forming v-nH complexes. The lifetime of positrons trapped in v-nH complexes gradually decreases with increasing number of H atoms, see Fig. 14. Up to 2 N or O atoms can be trapped in a vacancy. For a higher number of N or O atoms the complex becomes unstable. Lifetimes of positrons trapped in v-2N and v-2O complexes are 155 and 166 ps, respectively, i.e. significantly shorter compared to v-N and v-O.

Calculated momentum distributions of annihilating electron-positron pairs plotted in Figs. 19, 22 show that the positrons annihilated in the vicinity of N atoms leads to a peak located at $p_L \approx 20 \times 10^{-3} m_0 c$ due to contribution of nitrogen p electrons. This peak is even more pronounced for oxygen, which contains one more p electron. On the other hand, this peak is not present for a vacancy associated with H atoms due to lack of p electrons, see Fig. 15. Because of the peak at $p_L \approx 20 \times 10^{-3} m_0 c$ in the momentum distribution, positrons trapped in a v-N complex exhibit an enhanced contribution in the high momentum range compared to v-nH complexes. For v-O complexes, this high momentum contribution is enhanced even more. Hence, positron trapping in v-O or v-N complexes will result in a higher W parameter compared to v-nH complexes. For the sake of comparison with the experiment, the S and W parameters were calculated by integration of the calculated momentum distribution curves in the low and high momentum ranges and are shown for a perfect Nb lattice and various defects in a S-W correlation plot in Fig. 8. Note that agreement of

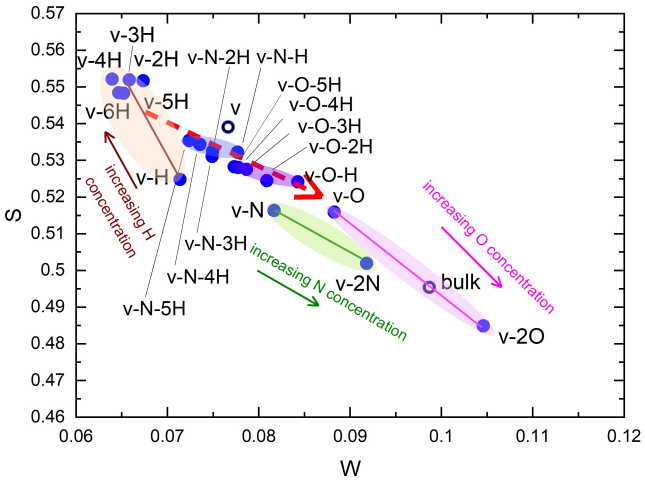

FIG. 8. Correlation S-W plot of S and W parameters calculated for positrons delocalized in perfect Nb lattice (bulk) and positrons trapped in various defects. Filled areas indicate regions in the S-W plane where various families of vacancy-impurity complexes are located, namely v-nH, v-nN, v-nO, v-N-nH and v-O-nH.

calculated S and W parameters with experiment is only qualitative due to limited accuracy of calculation of momentum distribution using atomic orbitals and also because in real sample only fraction of positrons is trapped at defects while others are annihilated in the free state. Nevertheless, calculated S,W parameters are useful for interpretation of trends observed in experiment.

IV. DISCUSSION

The XRR measurements showed that the Nb_2O_5-layer on Nb(100) completely dissolves at 523 K after already 1 h annealing. Further, at 573 K after 50 min the NbO_2-layer decomposes entirely into NbO [58]. At the same time, the diffuse scattering signal from interstitial oxygen measured by XRD in the near-surface region is decreasing drastically [34, 58]. This result is in agreement with [59], where it has been shown on polycrystalline

fine-grain niobium that heat treatment around 573 K for a few hours has been accompanied by an influx of oxygen at 0.1 at.%. This general agreement is important, as the XRR and XRD measurements were done on single crystal samples, and the diffusion in niobium is grain boundary dominated. It is possible that the exact temperature at which the Nb_2O_5-layer dissociates depends on the grain orientation and could also be affected by the existence of grain boundaries. The fact that on fine-grain samples the nature of the vacancy-complexes change between 473 K and 523 K indicate that the result of the XRR measurements from the Nb(100) sample are substantial to further discuss and interpret the observed effects in the positron annihilation spectroscopy measurements.

The S-W plot from Fig. 4 can now be easily understood taking into account the calculated S and W values from Fig. 8 and the XRR results. As shown in [56], the data points on the line up to 470 K are vacancy-hydrogen complexes that start to dissociate above 343 K, which is a critical temperature for the Nb-H system [60]. Above 473 K, the decomposition of the Nb_2O_5-layer releases O atoms, which diffuses into the Nb sub-surface region. From the inspection of Fig. 8 it is clear that v-O complexes are characterized by the S parameter comparable to v-H complexes but exhibit a remarkably larger W parameter. Hence, the shift of the experimental S-W points in Fig. 4 to larger W values occurring after annealing at 523 K can be explained by oxygen trapping at vacancies, i.e. transformation of v-H (or v) to v-O complexes. Hence, during the annealing of the Nb samples the nature of vacancy-type defects changes in the sequence v-nH ($T \leq 420$ K) $\rightarrow$ v (420 K $< T \leq$ 470 K) $\rightarrow$ v-O ($T \geq 520$ K) as indicated by the dashed line in Fig. 8. The *ab-initio* calculations also revealed that O atoms are bound to vacancies stronger than hydrogen. Therefore, H is prevented from returning to those positions in the lattice once the niobium cools down after annealing. This is another interesting observation, as hydrogen at vacancies act as niobium hydride nucleation centers when cooling down to cryogenic temperatures, which then causes an increase of the surface losses [35, 56, 61].

Using the results of *ab-initio* calculations, the experimental lifetime τ_2 corresponding to positrons trapped at various types of vacancy defects (Fig. 6) can be easier discussed. At temperatures below 390 K, τ_2 corresponds to a lifetime of positrons trapped in vacancies associated with multiple H atoms, whereas above 390 K, τ_2 gradually increases towards the lifetime for a bare vacancy. It indicates that during annealing at temperatures above 400 K, hydrogen atoms are gradually released from vacancies.

Since niobium is arranged in a bcc lattice, and the first native oxide-layer on top, NbO, is ordered in an fcc arrangement, a misalignment when stacking those two unit-cells onto each other appears. Depending on the atomic radius of the participating elements, the layer thickness, Nb-lattice orientation, internal stress and growth temperature, energetic optimal misalignment angles exist. For fcc - bcc interfaces, three orientations are predicted by the rigid-lattice theory and observed for many metal on metal systems, e.g. for Nb(100) the optimal in-plane relation to the NbO(110) cell, results in a tilt of 5.26° between the rows of $[101]_{fcc}$ with respect to $[001]_{bcc}$ [58, 62–64].

Measurements conducted by Delheusy et al. [58] show that the in-plane orientation of this interface for regular niobium used for SRF applications prior to any anneal does not show the optimal relation: neither is the NbO layer fully structured, nor is the orientation close to the optimal angle. According to these studies conducted, only an annealing at temperatures around 570 K provides enough thermal energy that the interface reorganizes itself in a way, such that it aligns closer to the theoretical optimum. Additionally, the lattice transition changes by creating an intermediate Nb_2O-layer as a buffer between the Nb and NbO lattice. An important consequence of the reduction of the lattice mismatch is that the vacancy concentration decreases in the niobium-oxide layer. This may have an impact on the detailed density of states (DOS), which may be phenomenologically represented by the so-called Dynes states. Dynes states help describe a realistic superconducting gap, where those states may arise from pair-breaking scattering [4, 65, 66]. Hence a reorganization and reduction of scattering sites will improve the ordering of the superconductor and should increase the superconducting gap. This is in agreement with the observed increase of the $\frac{\Delta}{k_b}$ ratio measured on Nb cavities after the Mid-T bake [22, 31, 67]. The onset of the overall defect density decrease in the sub-surface region is found at 523 K already according to our DB-PAS (Fig. 2)and PALS (Fig. 6) investigations, too.

Ma et al. [68] annealed niobium samples and came to the same observations as Delheusy et al. [58] and Semione et al. [34], that the Nb_2O_5-layer is dissolved at ≈ 550 K and that a Nb_2O-layer forms. Furthermore, from XPS measurements the reorganization and formation of the Nb_2O-layer accompanied by the occurrence of a new state in the valence-band was evidenced [68].

Although the Nb_2O_5-layer is polymorphous, structures (on the order of 10 nm) are observed with their symmetry matching that of the underlying nanocrystals, which are strongly influenced by the structural and electronic properties of the underlying NbO substrate [69]. Hence, a reorganization of the NbO-layer as seen by Ma et al., Delheusy et al. and Semione et al. and the subsequent regrowth of the Nb_2O_5-layer after the annealing on the newly ordered oxide will yields different vacancy concentration and properties for the pentoxide. Since it has been shown that oxide vacancies can cause surface magnetism [1–3], we inspected the surface of samples to test whether such an effect is observable. Indeed a multi-domain structure originating from niobium oxide was identified. This is a strong support for the existence of magnetic impurity and agrees with the conclusions and observations above, as a further impact on DOS is caused by magnetic impurities. A recent ab-initio study

by Sheridan et al. compared to X-ray absorption spectrum measurements by Harrelson et al. fully agree with our conclusions [70, 71]. In these reports, they confirm the presence of magnetic moments in the niobium oxides, caused by oxygen vacancies.

Impact on Accelerator Performance The RF losses of a cavity, given by the surface resistance R_s, is usually interpreted as the sum of two contributions:

$$R_s = R_{BCS}(E_{acc}, T) + R_{res}(E_{acc})$$

with R_{BCS} as the contribution derived by the microscopic theory of superconductors, and R_{res} is the residual resistance stemming from e.g. scattering processes on lattice defects or interstitials, dielectric losses in the native oxide and electric interface losses or trapped magnetic flux.

The correlation between RF induced losses and the existence of magnetic impurities, according to the Shiba theory [72], has been shown by Proslier et al. [6] already. Accompanying theoretical work showed that an inherent non-zero residual resistance R_{res} is a consequence of magnetic impurities in the RF penetration layer [7] and in general, the cause of any existing sub-gap states regardless of the microscopic origin. A more recent approach by Kubo et al. discusses different realistic surfaces, including Dynes sub-gap states and magnetic impurities in the material, further showing their potential to minimize RF losses and to modify the dynamic loss mechanisms if tailored accordingly [9, 66]. Hence, the proof of existence of magnetic domains in the oxide by the Kerr microscopy and the vacancy dynamics as shown above by the PALS measurement are well aligned with previous findings, and allow the microscopic identification of the origin of the magnetic impurities to be oxygen vacancies.

Another reduction of the RF induced losses at higher accelerating fields is possibly caused by the vacancy dynamics within the niobium. The annealing of niobium reduces the amount of vacancies in the near-surface region and also dissociates the hydrogen from those vacancies, which then are occupied by oxygen. Trapping of hydrogen on interstitial oxygen has been shown to be possible by our *ab-initio* calculations and also in [73], and was already used as a model to explain internal friction resonances in[74]. It is known that hydrogen trapped at vacancies can act as nucleation site of niobium hydrides upon cooling down. Assuming that the formation of niobium hydrides is suppressed once hydrogen is then trapped at interstitial oxygen, a reduction of lossy nanohydrides, and hence a reduction of the residual resistance at higher accelerating fields, is then the evident consequence.

Impact on Quantum Computing Cavities have a inherently a higher photon lifetime, due to the design and material used, by three orders of magnitude compared to other designs of qubits, offering a new approach in quantum computer design. In the work by Romanenko et al. [20, 21], the origin of the two-level systems reducing the photon lifetime were speculated to be within the oxide-layers, although no further discussion of their microscopic origin was given. The work by Sheridan et al. and Harrelson et al. [70, 71] suggest that oxygen deficient Nb_2O_5-layers are a significant source of the reduced coherence lifetime. In agreement to our findings of the reduced oxygen vacancies, the photon lifetime was improved for cavities which were annealed at 613 K.

V. CONCLUSION

In our study we investigated the dynamics of vacancies in niobium and its native oxide layer under annealing up to 573 K. Our results provide microscopic explanations of multiple observations from various research fields. The existence of magnetic impurities, caused by oxygen vacancies, are of interest for the quantum computing application, and our findings suggest that a reorganization of the oxide layer from which this application benefits during the anneal takes place.

In order to improve niobium surfaces for accelerating cavities, it is mandatory to fully understand the origin of various loss-contributions. The contribution to the residual resistance by magnetic impurities, caused by oxygen vacancies, can be manipulated by the anneal of Nb SRF cavities in the temperature range 573-673 K. At the same time, the observation of the vacancy-hydrogen complex dissociation and the formation of vacancy-oxygen complexes have a substantial impact on the interstitial hydrogen concentration. Hence, a reduction of the lossy nanohydrides and also the BCS resistance can originate from these processes, further explaining the improvements seen by the annealing.

[1] M. Venkatesan, C. B. Fitzgerald and J. M. D. Coey, Unexpected magnetism in a dielectric oxide, Nature 430 (2004).

[2] N. H. Hong, J. Sakai, N. Poirot and V, Brize, Room-temperature ferromagnetism observed in undoped semiconducting and insulating oxide thin films, Phys. Rev. B 73.13, 132404 (2006).

[3] M. Weissmann and L. A. Errico, The role of vacancies, impurities and crystal structure in the magnetic properties of TiO2, Physica B Condens. Matter 398.2, 179 (2007).

[4] R. C. Dynes, V. Narayanamurti, and J. P. Garno, Direct measurement of quasiparticle-lifetime broadening in a strong-coupled superconductor, Phys. Rev. Lett. 41, 21, (1978).

[5] T. Proslier, J. F. Zasadzinski, L. Cooley, C. Antoine, J. Moore, J. Norem, M. Pellin, and K. E. Gray, Tunneling study of cavity grade Nb: Possible magnetic scattering

at the surface, Appl. Phys. Lett. 92, 21, 212505 (2008).
[6] T. Proslier, M. Kharitonov, M. Pellin, J. Zasadzinski, G. Ciovati, Evidence of surface paramagnetism in niobium and consequences for the superconducting cavity surface impedance, IEEE Trans. Appl. Supercond. 21, 3, 2619 (2011).
[7] M. Kharitonov, T. Proslier, A. Glatz and M. J. Pellin, Surface impedance of superconductors with magnetic impurities, Phys. Rev. B 86, 024515 (20121).
[8] N.R. Groll, C. Becker, G. Ciovati, A. Grassellino, A. Romanenko, J.F.Zasadzinski and T.Proslier, Insight into bulk niobium superconducting RF cavities performances by tunneling spectroscopy, arXiv:1805.06359.
[9] T. Kubo and A. Gurevich, Field-dependent nonlinear surface resistance and its optimization by surface nanostructuring in superconductors, Phys. Rev. B 100, 6, 064522 (2019).
[10] J. Koch, T. M. Yu, J. Gambetta, A. A. Houck, D. I. Schuster, J. Majer, A. Blais, M. H. Devoret, S. M. Girvin and R. J. Schoelkopf, Charge-insensitive qubit design derived from the Cooper pair box, Phys. Rev. A 76, 4, 042319 (2007).
[11] J. A. Schreier, A. A. Houck, J. Koch, D. I. Schuster, B. R. Johnson, J. M. Chow, J. M. Gambetta, J. Majer, L. Frunzio, M. H. Devoret, S. M. Girvin and R. J. Schoelkopf, Suppressing charge noise decoherence in superconducting charge qubits, Phys. Rev. B 77, 18, 180502 (2008).
[12] A. A. Murthy, P. M. Das, S. M. Ribet, C. Kopas, J. Lee, M. J. Reagor, L. Zhou, M. J. Kramer, M. C. Hersam, M. Checchin, A. Grassellino, R. dos Reis, V. P. Dravid, A. Romanenko, Insights into Improving Performance of Niobium Superconducting Transmon Qubit Devices through Advanced Microscopy, arXiv:2203.08710.
[13] A. A. Murthy, P. M. Das, S. M. Ribet, C. Kopas, J. Lee, M. J. Reagor, L. Zhou, M. J. Kramer, M. C. Hersam, M. Checchin, A. Grassellino, R. dos Reis, V. P. Dravid, A. Romanenko, Potential nanoscale sources of decoherence in niobium based transmon qubit architectures, arXiv:2203.08710.
[14] D. A. Bennett, L. Longobardi, V. Patel, W. Chen, D. V. Averin and J. E. Lukens, Decoherence in RF SQUID qubits, Quantum Inf Process 8, 2, 217 (2009).
[15] G. Wendin, Quantum information processing with superconducting circuits: a review, Rep. Prog. Phys. 80, 10, 106001 (2017)
[16] C. Mueller, J. H. Cole and J. Lisenfeld, Towards understanding two-level-systems in amorphous solids: insights from quantum circuits, Rep. Prog. Phys. 82, 124501 (2019)
[17] D. Lee, J. L. DuBois and V. Lordi, Identification of the Local Sources of Paramagnetic Noise in Superconducting Qubit Devices Fabricated on Al2O3 Substrates Using Density-Functional Calculations, Phys. Rev. Lett. 112, 017001 (2014).
[18] N. Adelstein, D. Lee, J. L. DuBois, K. G. Ray, J. B. Varley and V. Lordi, Magnetic stability of oxygen defects on the SiO2 surface, AIP Advances 7, 025110 (2017).
[19] R. de Sousa, Dangling-bond spin relaxation and magnetic 1/f noise from the amorphous-semiconductor/oxide interface: Theory, Phys. Rev. B 76, 245306 (2007).
[20] A. Romanenko and D.I. Schuster, Understanding Quality Factor Degradation in Superconducting Niobium Cavities at Low Microwave Field Amplitudes, Phys. Rev. Let. 119, 264801 (2017).
[21] A. Romanenko, R. Pilipenko, S. Zorzetti, D. Frolov, M. Awida, S. Belomestnykh, S. Posen and A. Grassellino, Three-Dimensional Superconducting Resonators at T<20 mK with Photon Lifetimes up to $\tau = 2$s, Phys. Rev. Appl. 13, 034032 (2020).
[22] S. Posen, A. Romanenko, A. Grassellino, O.S. Melnychuk and D.A. Sergatskov, et al, Ultralow Surface Resistance via Vacuum Heat Treatment of Superconducting Radio-Frequency Cavities, Phys. Rev. Appl. 13, 1, 014024 (2020).
[23] J.T. Maniscalco, M. Ge, D. Gonnella, M. Liepe, Investigation of the Origin of the Anti-Q-Slope in North American Particle Accelerator Conference 2016, edited by M. Power, V. Shiltsev, V. R.W. Schaa, M. White, (JACOW, Chicago, 2016).
[24] M. Martinello, M. Checchin, A. Romanenko, A. Grassellino, S. Aderhold, S.K. Chandrasekeran, O. Melnychuk, S. Posen and D.A. Sergatskov, Field-enhanced superconductivity in high-frequency niobium accelerating cavities, Phys. Rev. Lett. 121, 22, 224801 (2018).
[25] B. P. Xiao, C.E. Reece and M.J. Kelley, Superconducting surface impedance under radiofrequency field, Physica C: Superconductivity 490, 26 (2013).
[26] A. Gurevich, Reduction of dissipative nonlinear conductivity of superconductors by static and microwave magnetic fields, Phys. Rev. Lett. 113, 8, 087001 (2014).
[27] R. Ballantini, A. Dacca, G. Gemme and R. Parodi, Improvement of the Maximum Field of Accelerating Cavities By Dry Oxidation in Proceedings of the 9th International Conference on RF Superconductivity (JACOW, Santa Fe 1999).
[28] F. Herman, and R. Hlubina, Microscopic interpretation of the Dynes formula for the tunneling density of states, Phys. Rev. B 94, 14, 144508 (2016).
[29] F. Herman and R. Hlubina, Microwave response of superconductors that obey local electrodynamics Phys. Rev. B 104, 9, 094519 (2021).
[30] F. He, W. Pan, P. Sha, J. Zhai, Z. Mi, X. Dai, S. Jin, Z. Zhang, C. Dong, B. Liu, H. Zhao, R. Ge, J. Zhao, Z. Mu, L. Du, L. Sun, L. Zhang, C. Yang and X. Zheng, Medium-temperature baking of 1.3 GHz superconducting radio frequency single-cell cavity, Supercond. Sci. Technol. 34,9, 095005 (2021).
[31] H. Ito, H. Araki, K. Takahashi and K. Umemori, Influence of Furnace Baking on QE Behavior of Superconducting Accelerating Cavities, Prog. Theor. Exp. Phys. 7, (2021).
[32] L.G. Parratt, Surface Studies of Solids by Total Reflection of X-Rays. Phys. Rev. 95, 2, 359 (1954).
[33] A. Stierle. *FEWLAY: a software for fitting X-ray reflectivity curves.* andreas.stierle@desy.de
[34] G.D.L. Semione, A. Dangwal Pandey, S. Tober, J. Pfrommer, A. Poulain, J. Drnec, G. Schütz, T.F. Keller, H. Noei, V. Vonk, B. Foster and A. Stierle, Niobium near-surface composition during nitrogen infusion relevant for superconducting radio-frequency cavities, Phys. Rev. Accel. Beams 22, 10, 103102 (2019).
[35] A. Romanenko, F. Barkov, L.D. Cooley and A. Grassellino, Proximity breakdown of hydrides in superconducting niobium cavities, Supercond. Sci. Technol. 26, 035003 (2013).
[36] J. Čížek, Characterization of lattice defects in metallic materials by positron annihilation spectroscopy: A review, J. Mater. Sci. Technol. 34, 577, (2018).

[37] Krause-Rehberg, R.& Leipner, H. S. *Positron annihilation in semiconductors: defect studies* (Springer-Verlag, 1999).

[38] J. Čížek, I. Prochazka, S. Danis, G. Brauer, W. Anwand, R. Gemma, E. Nikitin, R. Kirchheim, A. Pundt and R. K. Islamgaliev, Hydrogen-vacancy complexes in electron-irradiated niobium, Phys. Rev. B 79, 054108 (2009).

[39] W. Anwand, G. Brauer, M. Butterling, H.R. Kissener and A. Wagner, Design and construction of a slow positron beam for solid and surface investigations, Defect Diffus. Forum 331, 25 (2012).

[40] M. O. Liedke, W. Anwand, R. Bali, S. Cornelius, M. Butterling, T. T. Trinh, A. Wagner, S. Salamon, D. Walecki, A. Smekhova, H. Wende and K. Potzger, Open volume defects and magnetic phase transition in Fe60 Al40 transition metal aluminide, J. Appl. Phys.117, 163908 (2015).

[41] A. Wagner, M. Butterling, M. O. Liedke, K. Potzger and R. Krause-Rehberg, Positron annihilation lifetime and Doppler broadening spectroscopy at the ELBE facility, AIP Conf. Proc. 1970, 40003 (2018).

[42] PALSfit3, Version 3.218 `http://palsfit.dk/`.

[43] Origin(Pro), Version 2019b, OriginLab Corporation, Northampton, MA, USA.

[44] G. Kresse, J. Hafner, Ab initio molecular dynamics for liquid metals, Phys. Rev. B 47, 558 (1993).

[45] G. Kresse, J.Furthmüller, Efficient iterative schemes for ab initio total-energy calculations using a plane-wave basis set, Phys. Rev. B 54, 11169 (1996).

[46] J. P. Pedrew and A. Zunger, Self-interaction correction to density-functional approximations for many-electron systems, Phys. Rev. B 23, 5048 (1981).

[47] J. P. Pedrew, Electronic Structure of Solids 1991, edited by P. Ziesche and H. Eschrig (Akademie Verlag, Berlin, 1991), Vol.11.

[48] H. J. Monkhorst and J. D. Pack, Special points for Brillouin-zone integrations, Phys. Rev. B 13, 5188 (1976).

[49] M.J. Puska and R.M. Nieminen, Theory of Positrons in Solids and on Solid-Surfaces, Rev. Mod. Phys. 66, 841 (1994).

[50] M. Alatalo, B. Barbiellini, M. Hakala, H. Kauppinen, T. Korhonen, M.J. Puska, K. Saarinen, P. Hautojärvi and R.M. Nieminen, Theoretical and experimental study of positron annihilation with core electrons in solids, Phys. Rev. B 54, 2397 (1996).

[51] J. Kuriplach, A. L. Morales, C. Dauwe, D. Segers and M. Sob, Vacancies and vacancy-oxygen complexes in silicon: Positron annihilation with core electrons, Phys. Rev. B 58, 10475 (1998).

[52] S. Aderhold, S. Chel, E. Elsen, F. Eozénou, L. Lilje and D. Reschke, Cavity Process, ILC HiGrade Reports (2015)

[53] D. Reschke, V. Gubarev, J. Schaffran, L. Steder, N. Walker, M. Wenskat, and L. Monaco, Performance in the vertical test of the 832 nine-cell 1.3 GHz cavities for the European X-ray Free Electron Laser, Phys. Rev. Accel. Beams 20, 042004 (2017).

[54] The Technical Design Report of the European XFEL, edited by M. Altarelli, R. Brinkmann, M. Chergui, W. Decking, B. Dobson, S. Düsterer, G. Grübel, W. Graeff, H. Graafsma, J. Hajdu, J. Marangos, J. Pflüger, H. Redlin, D. Riley, I. Robinson, J. Rossbach, A. Schwarz, K. Tiedtke, T. Tschentscher, I. Vartaniants, H. Wabnitz, H. Weise, R. Wichmann, K. Witte, A. Wolf, M. Wulff, M. Yurkov (DESY XFEL Project Group and European XFEL Project Team and Deutsches Elektronen-Synchrotron, Hamburg, 2007).

[55] W. Singer, X. Singer, A. Brinkmann, J. Iversen, A. Matheisen, A. Navitski, Y. Tamashevich, P. Michelato and L. Monaco, Production of superconducting 1.3-GHz cavities for the European X-ray Free Electron Laser, Phys. Rev. Accel. Beams 19, 092001 (2016).

[56] M. Wenskat, J. Cizek, M. O. Liedke, M. Butterling, C: Bate, P. Hausild, E. Hirschmann, A. Wagner and Hans Weise , Vacancy-Hydrogen Interaction in Niobium during Low-Temperature Baking, Sci. Rep. 10, 1 (2020).

[57] H. Padamsee, J. Knobloch, and T. Hays, T. RF superconductivity for accelerators, edited by (Wiley-VCH Verlag, Weinheim, 2008), 2nd Edition

[58] Delheusy, Melissa. "X-ray investigation of Nb/O interfaces." Thesis, Universität Stuttgart (2008).

[59] E. M. Lechner, J. W. Angle, F. A. Stevie, M. J. Kelley, C. E. Reece, and A. D. Palczewski, RF surface resistance tuning of superconducting niobium via thermal diffusion of native oxide, Appl. Phys. Lett. 119, 8 (2021).

[60] M. W. Stanley and Z.C. Szkopiak, The α and β peaks in cold-worked niobium, J. Mater. Sci. 2, 6, 559 (1967).

[61] P.G. De Gennes and J.P. Hurault, Proximity effects under magnetic fields. II - Interpretation of breakdown, Physics Letters 17, 181 (1965).

[62] Z. Nishiyama, Sci. Rept. Tohoku Univ. 23, 638 (1934).

[63] G. Wassermann, Influence of the $\alpha - \gamma$ transformation of an irreversible Ni steel onto crystal orientation and tensile strength, Arch. Eisenhüttenwes. 126, 647 (1933).

[64] Y. Gotoh and M. Uwaha, Geometrical Interpretation of the Interfacial Energy between bcc and fcc Lattices and Preferred Orientation Relationship of the Epitaxy, Jpn. J. Appl. Phys. 26, 1A, L17 (1987).

[65] H. Boschker, E. Fillis-Tsirakis, C. Richter, D. Zhang, J. Smet and L. Kuerten, Microscopic origin of the Dynes parameter Γ of the LaAlO3 – SrTiO3 interface superconductor, Phys. Rev. B 102, 134506 (2020).

[66] T. Kubo, Effects of nonmagnetic impurities and subgap states on the kinetic inductance, complex conductivity, quality factor and depairing current density, Phys. Rev. Applied 17, 014018 (2022).

[67] M. Wenskat, Vacancy-Hydrogen Dynamics and Magnetic Impurities During Mid-T Bake, in Proceedings of the 20th International Conference on RF Superconductivity, edited by K. Saito, T. Xu, N. Sakamoto, Y. Lesage, V.R.W. Schaa (JACOW, East Lansing, 2021).

[68] Q. Ma, P. Ryan, J. W. Freeland and R. A. Rosenberg, Thermal effect on the oxides on Nb (100) studied by synchrotron-radiation x-ray photoelectron spectroscopy, J. Appl. Phys. 96, 12, 7675 (2004).

[69] K. Zhussupbekov, K. Walshe, S. I. Bozhko, A. Ionov, K. Fleischer, E. Norton, A. Zhussupbekova, V. Semenov, I. V. Shvets and B. Walls, Oxidation of Nb (110): atomic structure of the NbO layer and its influence on further oxidation, Sci. Rep. 10, 1, 1 (2020).

[70] E. Sheridan, T. F. Harrelson, E. Sivonxay, K. A. Persson, M. Virginia P. Altoé, I. Siddiqi, D. F. Ogletree, D. I. Santiago, S. M. Griffin, Microscopic Theory of Magnetic Disorder-Induced Decoherence in Superconducting Nb Films, arXiv:2111.11684.

[71] T. F. Harrelson, E. Sheridan, E. Kennedy, J. Vinson, A. T. N'Diaye, M. Virginia, P. Altoe, A. Schwartzberg, I. Siddiqi, D. F. Ogletree, M. C. Scott and S. M. Griffin, Elucidating the local atomic and electronic structure of amorphous oxidized superconducting niobium films,

Appl. Phys. Lett. 119, 24, 24404 (2021).
[72] H. Shiba, A hartree-fock theory of transition-metal impurities in a superconductor, Prog. Theor. Phys. 50, 1, 50 (1973).
[73] D. C. Ford, L.D. Cooley and D.N. Seidman, Suppression of hydride precipitates in niobium superconducting radio-frequency cavities, Supercond. Sci. Technol. 26, 10, 105003 (2013).
[74] P. Schiller and A. Schneiders, On the hydrogen relaxation peak in niobium, Phys. Status Solidi 29, 2, 375 (1975).
[75] K. Saarinen, P. Hautojarvi, C. Corbel, Chapter 5: Positron Annihilation Spectroscopy of Defects in Semiconductors, in Identification of Defects in Semiconductors, edited by M. Stavola (Elsevier, 1998).
[76] O.E. Mogensen, Positronium formation in condensed matter and high-density gases, in 6. International Conference on Positron Annihilation, edited by P.G. Coleman, S.C. Sharma, L.M. Diana, (Amsterdam, 1982).
[77] M. Charlton, and J.W. Humberston, Positron Physics (Cambridge Univ. Press, Cambridge 2001).
[78] C.H. Hodges and M.J. Stott, Work Functions for Positrons in Metals, Phys. Rev. B 7, 73 (1973).
[79] S. J. Tao, Positronium annihilation in molecular substances, J. Chem. Phys. 56, 54995510 (1972).
[80] M. Eldrup, D. Lightbody and J.N. Sherwood, The temperature-dependence of positron lifetimes in solid pivalic acid, Chem. Phys. 63, 5158 (1981).
[81] M. Deutsch, E. Dulit, Short range interaction of electrons and fine structure of positronium, Phys. Rev. 84, 3, 601 (1951).
[82] M. Deutsch, S.C. Brown, Zeeman effect and hyperfine splitting of positronium Phys. Rev. 85, 6, 1047 (1952).
[83] O. Halpern, Magnetic quenching of the positronium decay, Phys. Rev. 94, 4, 904 (1954).
[84] P. Moskal, D. Kisielewska, C. Curceanu, E. Czerwinski, K. Dulski, A. Gajos, M. Gorgol, B. Hiesmayr, B. Jasinska and K. Kacprzak, Feasibility study of the positronium imaging with the J-PET tomograph, Phys Med Biol. 64, 5, 055017 (2019).
[85] E. Boroński and R.M. Nieminen, Electron-positron density-functional theory, Phys. Rev. B 34, 3820 (1986).
[86] T. Korhonen, M.J. Puska and R.M. Nieminen, First-principles calculation of positron annihilation characteristics at metal vacancies, Phys. Rev. B 54, 15016 (1996).
[87] D.C. Ford, P. Zapol and L.D. Cooley, First-Principles Study of Carbon and Vacancy Structures in Niobium, J. Phys. Chem. C 119, 14728 (2015).
[88] W. Frank, U. Breier, C. Elsässer and M. Fähnle, Properties of monovacancies and self-interstitials in bcc Li: An ab-initio pseudopotential study, Phys. Rev. B 48, 7676 (1993).
[89] T. Beuerle, R. Pawellek, C. Elsässer and M. Fähnle, The influence of the atomic-sphere approximation on the calculation of the vacancy formation energy of Li, J. Phys. Condens. Matter 3, 1957 (1991).
[90] P. Hautojarvi, H. Huomo, M.J. Puska and A. Vehanen, Vacancy recovery and vacancy-hydrogen interaction in niobium and tantalum studied by positrons, Phys. Rev. B 32, 4326 (1985).
[91] D.C. Ford, L.D. Cooley and D.N. Seidman, First-principles calculations of niobium hydride formation in superconducting radio-frequency cavities, Supercond. Sci. Technol. 26, 095002 (2013).
[92] J.A. Pryde and C.G. Titcomb, Thermodynamic data of the hydrogen-niobium system, J. Phys. C: Solid Stat Phys. 5, 1301 (1972).
[93] J. Čížek, I. Procházka, F. Bečvář, R. Kužel, M. Cieslar, G. Brauer, W. Anwand, R. Kirchheim and Astrid Pundt, Hydrogen-induced defects in bulk niobium, Phys. Rev. B 69, 224106 (2004).
[94] A. Pundt and R. Kirchheim, Hydrogen in metals: microstructural aspects, Annu. Rev. Mater. Sci. 36, 555 (2006).
[95] Y. Tateyama and T. Ohno, Stability and clusterization of hydrogen-vacancy complexes in α-Fe: An *ab initio* study, Phys. Rev. B 67, 174105 (2003).
[96] K. Ohsawa, J. Goto, M. Yamakami, M. Yamaguchi and M. Yagi, Trapping of multiple hydrogen atoms in a tungsten monovacancy from first principles, Phys. Rev. B 82, 184117 (2010).
[97] J. Dryzek and P. Horodek, GEANT4 simulation of slow positron beam implantation profiles, Nucl. Instrum. Methods Phys. Res. B 266, 4000 (2008).

VI. ACKNOWLEDGEMENTS

The authors of this work thank A. Ermakov and S. Sievers (DESY) for their support in the preparation of the samples. The DESY affiliated authors acknowledge support from DESY (Hamburg, Germany), a member of the Helmholtz Association HGF. Positron annihilation lifetime studies were carried out at the ELBE facility at the Helmholtz-Zentrum Dresden-Rossendorf. The authors thank the facility staff for their assistance. The authors also thank the ESRF for the granted beamtime under to carry out the X-ray reflectivity measurements. The UHV-induction annealing of the Nb crystals used in the XRR measurements by T. Meisner and A. Weible at the MPI for Intelligent Systems is acknowledged. This work was supported by the BMBF under the research grant 05H18GURB1, the Impulse-und Networking fund of the Helmholtz Association (VH-VI-442 Memriox), and the Helmholtz Energy Materials Characterization Platform (03ET7015). Computational resources for the DFT calculations were supplied by the project "e-Infrastruktura CZ" (e-INFRA LM2018140) provided within the program Projects of Large Research, Development and Innovations Infrastructures.

VII. COMPETING INTERESTS

The authors declare no competing interests.

VIII. AUTHOR CONTRIBUTIONS

M.W. conceived the idea and the study, performed experiments, analyzed data, wrote the manuscript and supervised the project. J.C. carried out DFT calculations, analyzed data and wrote the manuscript. M.O.L.

performed PALS and PAS experiments, analyzed data and wrote the manuscript. M.B. performed PALS experiments, analyzed data and wrote the manuscript. M.S. carried out Kerr microscopy and analyzed data under supervision of M.A.. G.D.L.S. prepared samples, carried out the X-ray reflectivity measurements and analyzed data under supervision of A.S.. Co.B. carried out Kerr microscopy. C.B. prepared the samples and performed experiments. O.M. carried out DFT calculations. E.H. performed PALS experiments and contributed to the experimental design. A.W. contributed to the experimental design performed PALS experiments. H.W., A.S., M.A., W.H. contributed to the experimental design, discussed results and reviewed the manuscript.

Appendix A: Surface treatment of samples

The baseline treatment for the samples were:

1. Electro-polishing (EP) with a total removal of 120 µm surface layer
2. Ultra-sonic Cleaning and High Pressure Rinsing (DI Water with 100 bar)
3. 1073 K annealing for 3 hours at a pressure below 10^{-5} mbar
4. Electro-polishing with a total removal of 30 µm surface layer
5. Ultra-sonic Cleaning and High Pressure Rinsing (DI Water with 100 bar)

The electro-poslishing was done with HF (w=40%) and H_2SO_4 (w=98%) acids mixed in the volume ratio 1:9. Dedicated sample chemistry and high pressure rinsing holders have been developed to use the standard infrastructure for cavity treatment at DESY. The final preparation step, the annealing, was then studied *in-situ* using methods described above.

Appendix B: Details on positron annihilation spectroscopy

The Doppler shift of the annihilation radiation is determined by the momentum of the electron which annihilated the positron. In DB spectroscopy, the broadening of the annihilation photo-peak is characterized in terms of the line shape parameters S (sharpness) and W (wing) which contain information about the contributions of annihilation by low or high momentum electrons, respectively. The S parameter is defined as the ratio of the central area A_1 of the annihilation photo-peak to the total peak area A_{total}, see Fig. 9. In the present work, the energy range $\delta E = \pm 0.93\,\mathrm{keV}$ around the annihilation peak was used for calculation of the S parameter. Positrons annihilated by free electrons, which on average

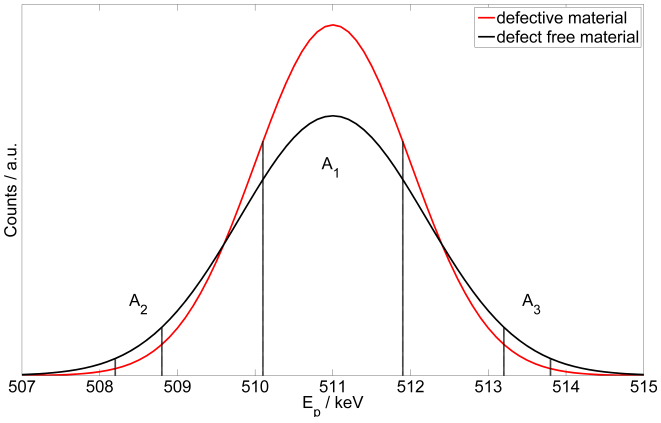

FIG. 9. Positron annihilation photo-peak in a metallic material. The central area $A_1$is used to quantify the S-parameter, while the areas A_2 and A_3 are used for the W-parameter. Changes in the density, type and chemical environment of positron traps change the momentum distribution of electrons annihilating positrons and hence lead to different values of the S and W parameters.

have a low momentum, contribute to the central region of the annihilation photo-peak. An increase of vacancies will lead to a higher fraction of positrons getting trapped and annihilated by free electron in these vacancies and therefore cause an increase of the S parameter. The W-parameter is the fractional area in the wing regions A_2 ($508.56 \pm 0.35\,\mathrm{keV}$) and A_3 ($513.44 \pm 0.35\,\mathrm{keV}$), and represents a measure of positrons annihilated by core electrons of the surrounding elements. The core electrons have on average a higher momentum, causing an element characteristic contribution in the momentum distribution. Hence, the correlated measurement of S- and W-parameters is sensitive to the type and the atomic environment of positron trapping sites or defects in the material. Plotting S and W-parameters as a trajectory in the S-W plane provides a powerful approach to interpret the depth profiling data. In samples containing single type of defects, the points generally fall on a line segment because only two states of positrons (free positron and positron trapped at defect) are formed. The measured S and W represent a superposition of contributions from these states and fulfill a linear relationship

$$(S - S_{bulk}) = R \cdot (W - W_{bulk}) \tag{B1}$$

with a defect-specific slope R [75]. The symbols S_{bulk} and W_{bulk} stand for the S and W-parameter of a defect-free sample of the same material. In the case of slow positron beam experiments the positrons are implanted into films with defined kinetic energy E_p typically in the range of few tens of eV up to several tens of keV, which enables depth profiling. A mean positron implantation depth can be approximated by a simple material density dependent formula [97]

$$\langle z \rangle = \frac{A}{\rho} \cdot {E_p}^n, \tag{B2}$$

where $A = 36$ and $n = 1.62$ are empirically acquired values and ρ is the material density.

Positrons implanted into solids may form hydrogen-like bound state with an electron called positronium (Ps) [76, 77]. Ps is formed on external or internal surfaces of solids by a thermalized positron picking an electron on the surface and escaping from solid into a pore or free space [78]. Depending on the orientation of electron and positron spin in the bound state, Ps decays in two photons (para-Ps, singlet-state) or three photons (ortho-Ps, triplet-state). In solids the three photon decay of ortho-Ps is suppressed due to pick-off annihilation (two photon decay) with an electron with opposite spin from the environment [79, 80]. Three photon decay can be suppressed also by magnetic field [81–84], in particular by ortho-to-para conversion of Ps in the vicinity of paramagnetic species. Hence, the ratio of the "$3\gamma/2\gamma$" is sensitive to the chemical environment of the Ps atom.

Appendix C: Details on the *ab-initio* calculations

Since hydrogen is a light atom, vibrational energy of hydrogen ions in the Nb lattice has to be considered. Zero-point energy (ZPE) of hydrogen was calculated using the Einstein model for localized hydrogen modes, i.e. by summing up the vibration energies of hydrogen normal modes, $\mathrm{ZPE} = \frac{1}{2}\sum_i h\nu_i$, where h is the Planck constant. The vibration frequencies ν_i were determined from the energy versus displacement curves of hydrogen atoms.

Positron annihilation observables were calculated using DFT within the so-called standard scheme [49]. In this approximation, the positron density is assumed to be negligibly small everywhere and not affecting the bulk electron structure. At first, the electron density $n(\boldsymbol{r})$ in the material is solved without the positron. Subsequently, the effective potential for a positron is constructed as

$$V_+(\boldsymbol{r}) = \phi(\boldsymbol{r}) + V_{corr}[n] \tag{C1}$$

where $\phi(\boldsymbol{r})$ is the Coulomb potential produced by the charge distribution of electrons and nuclei and V_{corr} is the zero positron density limit of the electron-positron correlation potential [49]. The ground state positron wave function was calculated by a numerical solution of the single particle Schrödinger equation

$$-\frac{1}{2}\nabla^2\psi_+(\boldsymbol{r}) + V_+(\boldsymbol{r})\psi_+(\boldsymbol{r}) = E_+\psi_+(\boldsymbol{r}), \tag{C2}$$

where E_+ is the positron ground state energy.

The positron lifetime τ was calculated from the overlap of the positron density $n_+(\boldsymbol{r}) = |\psi_+(\boldsymbol{r})|^2$ and the electron density $n(\boldsymbol{r})$ using the expression

$$\frac{1}{\tau} = \pi r_e^2 c \int n_+(\boldsymbol{r}) n(\boldsymbol{r}) \gamma[n]\, d\boldsymbol{r}, \tag{C3}$$

where r_e is the classical electron radius, and c is the speed of light. The electron enhancement factor γ accounts for the pile-up of electrons at the positron site [49]. The electron-positron correlation potential and the enhancement factor were treated within local density approximation (LDA) using the parametrization by Boroński and Nieminen [85]. A Brillouin-zone integration over the lowest-lying positron state [86] was used in the calculations of the positron density for vacancies to achieve rapid convergence of the results with respect to the supercell size.

The momentum distribution of the annihilating electron-positron pairs was calculated using the approach described in Refs. [50, 51]. The contribution $\varrho^{i,nl}$ from the i-th atom and a shell characterized by the principal and orbital quantum numbers N, l was calculated by the formula

$$\varrho^{i,Nl}(p) = 4\pi^2 r_e^2 c N_e^{i,Nl} \gamma^{i,Nl} \left| \int R_+^i R_-^{i,Nl} B_l(pr) r^2 dr \right|^2, \tag{C4}$$

where $N_e^{i,Nl}$ denotes the number of electrons in the (N, l) shell, B_l is a spherical Bessel function and R_+^i, $R_-^{i,Nl}$ denote the radial part of the positron and electron wave functions. A state-dependent positron enhancement factor $\gamma^{i,Nl}$ is used in the calculation [51]. The momentum distribution of the annihilating electron-positron pairs was obtained by summing the partial contributions $\varrho^{i,Nl}(p)$ over all the occupied atomic sites and filled electron shells. Since the core electrons localized in atomic shells are practically not affected by crystal bonding and retain their atomic character, the present approach describes well the high-momentum part of the momentum distribution ($p > 10^{-3}\ m_0c$), where the contribution of positrons annihilated by core electrons dominates. To mimic the effect of the finite resolution of the experimental setup, the theoretical momentum distribution curves were convoluted with a Gaussian function with a FWHM of $3.5 \times 10^3\ m_0c$. For the sake of comparison with the experiment, the calculated momentum distributions are presented as ratio curves related to the momentum distribution calculated for a perfect Nb crystal. Calculations of positron observables were always performed for relaxed geometries of defects obtained from VASP calculations.

1. Pure Nb

As a benchmark, we calculated the bulk positron lifetime, i.e. lifetime of a positron delocalized in a perfect (defect-free) Nb lattice of 128 ps. This value is in good agreement with experiment [38].

The formation energy of a vacancy in Nb was calculated from the expression

$$E_{f,v} = E[N-1, \mathrm{v}] - \frac{N}{N-1} E[N, \mathrm{bulk}], \qquad \text{(C5)}$$

where E[N,bulk] is the total energy of a perfect supercell consisting of $N = 128$ Nb atoms and E[N-1,v] is the energy of a supercell containing a vacancy. The calculated vacancy formation energy $E_f = 2.79$ eV is in good agreement with the value of 2.71 eV calculated by Ford et al. in Ref. [87] as well as with experimental values reported in literature, falling into the range 2.7-3.0 eV [88, 89]. The eight nearest neighbouring Nb ions surrounding the vacancy relax towards the vacancy. Their displacement from the rigid lattice sites is 0.13 Å. Fig. 10a shows the calculated positron density in the (001) plane containing a vacancy. The positron is confined in a vacancy and the positron density has a spherical symmetry with its center in the vacancy. Calculated lifetimes of a positron trapped in a vacancy is 207 ps. This calculated value is also in good agreement with the experimental lifetime of (210 ± 2) ps reported in literature [90].

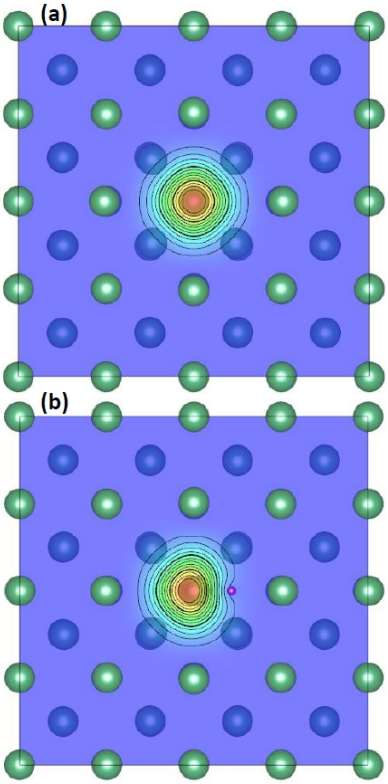

FIG. 10. Relaxed configuration of lattice ions and the calculated positron density in the (001) plane for (a) a vacancy, (b) a v-H complex.

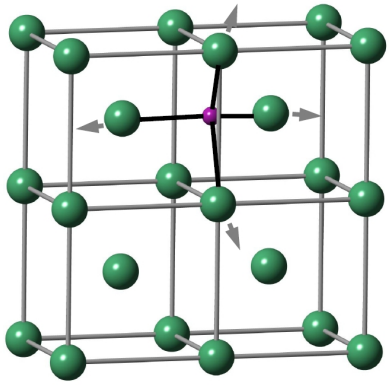

FIG. 11. Relaxed configuration of a hydrogen interstitial located in the tetrahedral interstitial site. Arrows show directions of ion relaxations.

2. Hydrogen in Nb

The lowest energy site of a hydrogen absorbed in the Nb lattice is the tetrahedral interstitial site. The Nb lattice around a hydrogen interstitial (H_i) is locally expanded. As shown in Fig. 11, Nb ions around H_i are displaced in the direction away of the hydrogen. The calculated displacement of the four nearest neighbour Nb ions surrounding H_i is 0.08 Å.

The formation energy of H_i, i.e. absorption energy for hydrogen in the tetrahedral site, was calculated as

$$E_{f,\mathrm{H}_i} = E[N, \mathrm{H}_i] + ZPE[\mathrm{H}_i] - \left(E[N, \mathrm{bulk}] + \frac{1}{2} ZPE[\mathrm{H}_2] \right), \tag{C6}$$

where $E[N, \mathrm{H}_i]$ is the total energy of the supercell containing hydrogen in the tetrahedral site, $ZPE[\mathrm{H}_i]$ and $ZPE[\mathrm{H}_2]$ denote the ZPE for a H_i and H_2 molecule, respectively. The hydrogen absorption energy was calculated using Eq. (C6) and the derived value $E_{f,\mathrm{H}_i} = -0.29$ eV is in good agreement with previous *ab-initio* calculations [91], as well as with experimental data [92]. The negative value of E_{f,H_i} indicates that the hydrogen absorption in Nb is an exothermic process.

The interaction of an interstitial hydrogen impurity with vacancies in Nb has been considered and it was found that there is an attractive interaction between H_i and the vacancy. Consequently, hydrogen is bound to a vacancy forming a so-called vacancy-hydrogen (v-H) complex. The lowest energy configuration of v-H complex is shown in Fig. 10b. The hydrogen impurity is located on the line between the vacancy and the nearest neighbour octahedral interstitial site and is displaced 0.23 Å from the octahedral site towards the vacancy. Hence, the distance of hydrogen from the center of vacancy is 1.43 Å. The hydrogen binding energy to the vacancy was calculated from the expression

$$E_{B,\text{v-H}} = E[N-1, \text{v-H}] + E[N, \mathrm{bulk}] + ZPE[\text{v-H}] - (E[N-1, \mathrm{v}] + E[N, \mathrm{H}_i] + ZPE[\mathrm{H}_i]), \tag{C7}$$

where $E[N-1, \text{v-H}]$ is the energy of the supercell containing a v-H complex in the lowest energy configuration and $ZPE[\text{v-H}]$ is the ZPE of hydrogen in the v-H complex. The calculated binding energy $E_{B,\text{v-H}} = -0.57$ eV is comparable to the binding energy calculated using the effective medium theory [93]. Note that a negative binding energy means that the attachment of hydrogen to a vacancy leads to a decrease of energy, i.e. hydrogen attached to a vacancy has a lower energy than hydrogen alone, located in tetrahedral interstitial site. Hence, hydrogen absorbed in Nb makes formation of vacancies easier. When the Nb lattice contains interstitial hydrogen, the vacancy formation energy is reduced to 2.79 – 0.57 = 2.22 eV due to hydrogen binding to vacancy.

Fig. 10b shows the calculated positron density in the (001) plane containing a v-H complex. Similarly to the bare vacancy, positrons are confined in a v-H complex, but the positron density exhibits a clear asymmetry due to repulsive interaction between the hydrogen ion and a positron. Hence, the calculated positron lifetime was reduced with respect to a bare vacancy down to 199 ps.

In many metals, vacancies are able to trap multiple hydrogen atoms forming v-nH complexes [38, 93–96]. For this reason, trapping of multiple hydrogen atoms in a Nb vacancy should be considered as well. The binding energy of additional hydrogen to a vacancy associated already with n hydrogen atoms leading to a transformation of a v-nH complex into a v-(n+1)H complex can be calculated as

$$\begin{aligned} E_{B,\text{v}-(n+1)\text{H}} = {} & E[N-1, \text{v-}(n+1)\text{H}] + E[N, \mathrm{bulk}] + ZPE[\text{v-}(n+1)\text{H}] \\ & - (E[N-1, \text{v-}n\text{H}] + E[N, \mathrm{H}_i] + ZPE[\text{v-}n\text{H}] + ZPE[\mathrm{H}_i]), \end{aligned}$$

where $E[N-1, \text{v-}(n+1)\text{H}]$ and $E[N-1, \text{v-}n\text{H}]$ is the energy of supercells containing v-($n+1$)H and v-nH complexes respectively, and $ZPE[\text{v-}(n+1)\text{H}]$, $ZPE[\text{v-}n\text{H}]$ are the corresponding ZPEs of hydrogen atoms attached to the vacancy. Calculated binding energies of hydrogen atoms to a vacancy are plotted in Fig. 12. In the lowest energy configuration, hydrogen atoms are always located on the lines between the vacancy and the nearest neighbour octahedral sites. Since there are six octahedral sites around a vacancy, the binding energy of hydrogen to a vacancy remains negative up to six atoms. Hence, a single vacancy is able to trap at least six hydrogen atoms forming v-6H complex. From an inspection of Fig. 12, it is clear that the absolute value of the hydrogen binding energy decreases with an increasing number hydrogen atoms attached to a vacancy. Hence, with an increasing number of hydrogen atoms the binding of an additional hydrogen atom becomes weaker and weaker due to an repulsive H-H interaction. Vacancies associated with n hydrogen atoms ($n \leq 6$) are still able to trap positrons. As an example, Fig. 13 shows the calculated positron density in the (001) plane for a v-2H and a v-4H complex. Although positrons are localized in v-nH complexes, deformations of the positron density due to the repulsion between positrons and hydrogen interstitials are clearly visible in Fig. 13.

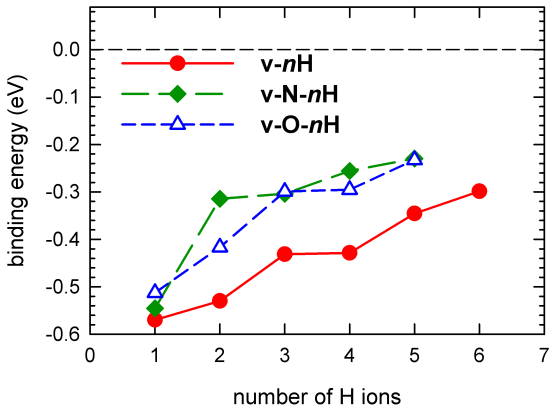

FIG. 12. Calculated binding energies of hydrogen atoms to a vacancy forming v-nH complexes and to vacancies associated already with N or O atoms forming v-N-nH or v-O-nH complexes.

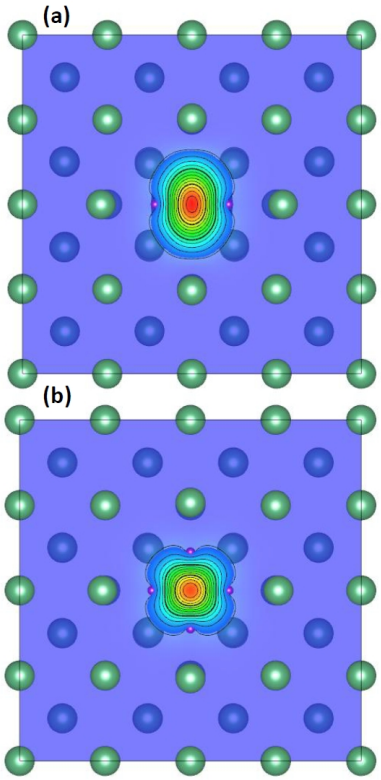

FIG. 13. Relaxed geometry of the lattice ions and the positron density in the (001) plane for (a) a v-2H complex, (b) a v-4H complex.

Fig. 14 shows calculated lifetimes of positrons trapped in v-nH complexes as a function of number n of H atoms bound to vacancy. Lifetime of trapped positrons gradually decreases towards the bulk positron lifetime with increasing number of H atoms attached to vacancy.

The calculated momentum distributions of annihilating

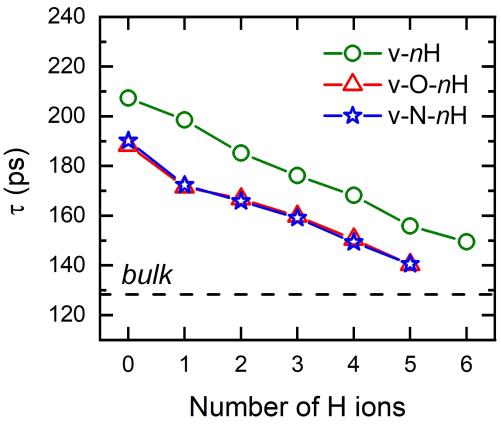

FIG. 14. Calculated lifetimes of positrons trapped at v-nH, v-N-nH and v-O-nH complexes as a function of the number n of hydrogen atoms attached to a vacancy. The bulk positron lifetime for Nb is indicated by dashed line.

electron-positron pairs for v-nH complexes, presented as ratio curves with respect to defect-free pure Nb, are plotted in Fig. 15. The impact of hydrogen on the momentum distribution is relatively weak. Positrons trapped in v-nH complexes are responsible for slightly enhanced contribution at $p_L \approx 15 \times 10^{-3}\ m_0c$. With an increasing number of hydrogen atoms, this contribution becomes more pronounced.

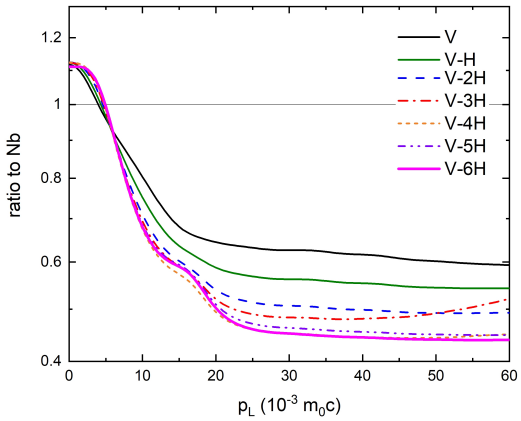

FIG. 15. Calculated momentum distributions for positrons trapped in v-nH complexes presented as ratio curves with respect to pure Nb.

3. Nitrogen in Nb

Our *ab-initio* calculations revealed that in contrast to hydrogen, nitrogen absorbed in the Nb lattice has lowest energy in the octahedral interstitial site. The Nb lattice is locally distorted around nitrogen interstitial (N_i) as

shown in Fig. 16, where a relaxation of the two nearest neighbors of N_i is outward (displacement 0.39 Å) while the four next nearest neighbours exhibit inward relaxation (displacement -0.11 Å). The formation energy of (N_i) was calculated from the expression

$$E_{f,\mathrm{N}_i} = E[N, \mathrm{N}_i] - \left(E[N, \mathrm{bulk}] + \frac{1}{2} E[\mathrm{N}_2] \right), \qquad \text{(C8)}$$

where $E[N, \mathrm{N}_i]$ is the energy of a supercell containing N_i in the octahedral position and $E[\mathrm{N}_2]$ is the energy of N_2 molecule. The negative formation energy $E_{f,\mathrm{N}_i} = -1.74$ eV indicates that nitrogen absorption into the Nb lattice is an exothermic process. Similarly to hydrogen, interstitial nitrogen impurities in the Nb lattice can be trapped at a vacancy. The equilibrium geometry of a complex of a vacancy associated with a nitrogen atom (v-N) is shown in Fig. 17. Similarly to hydrogen at a vacancy, nitrogen is also located on the line connecting a vacancy and the nearest neighbour octahedral site. The displacement of the nitrogen from the octahedral site towards the vacancy is 0.09 Å, i.e. smaller than that for hydrogen. The binding energy of nitrogen to a vacancy was calculated as

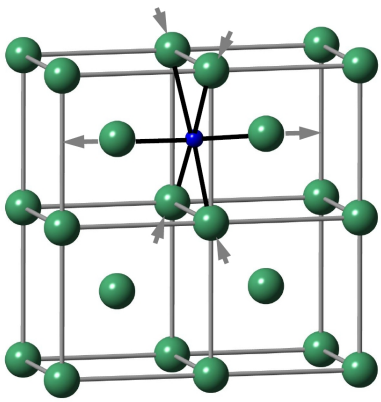

FIG. 16. Relaxed configuration of a nitrogen interstitial located in the octahedral interstitial site. Arrows show the directions of ion relaxations.

$$E_{B,\text{v-N}} = E[N-1, \text{v-N}] + E[N, \mathrm{bulk}] - (E[N-1, \mathrm{v}] + E[N, \mathrm{N}_i]), \qquad \text{(C9)}$$

where $E[N-1, \text{v-N}]$ is the energy of a supercell containing a v-N complex. This binding energy $E_{B,\text{v-N}} = -0.37$ eV is less negative compared to that for hydrogen indicating that nitrogen binding to vacancy is weaker than for hydrogen. Nevertheless, similarly to hydrogen, nitrogen absorbed in the Nb lattice facilitates the formation of vacancies and reduces the vacancy formation energy to $2.79 - 0.37 = 2.42$ eV. The calculated positron density in the (001) plane containing a v-N complex is plotted in Fig. 17a. A positron is confined in a v-N complex, however, the asymmetry of the positron density due to a repulsion between the positron and the nitrogen is more pronounced compared to a v-H complex. Also the shortening of the positron lifetime compared to a bare vacancy is more pronounced and the calculated lifetime of positrons trapped in a v-N complex is 190 ps. Trapping of multiple nitrogen atoms in a vacancy has also been considered. The binding energy of an additional nitrogen atom to a vacancy associated already with n nitrogen atoms is given by the expression

$$E_{B,\text{v-}(n+1)\text{N}} = E[N-1, \text{v-}(n+1)\text{N}] + E[N, \mathrm{bulk}] - (E[N-1, \text{v-}n\text{N}] + E[N, \mathrm{N}_i]), \qquad \text{(C10)}$$

where $E[N-1, \text{v-}(n+1)\text{N}]$ and $E[N-1, \text{v-}n\text{N}]$ represent the energy of a supercell containing v-$(n+1)$N and v-nN complexes, respectively. The calculated binding energy is plotted in Fig. 18 as a function of the number of nitrogen atoms bound to a vacancy. From an inspection of the figure it is clear that the binding energy is only negative

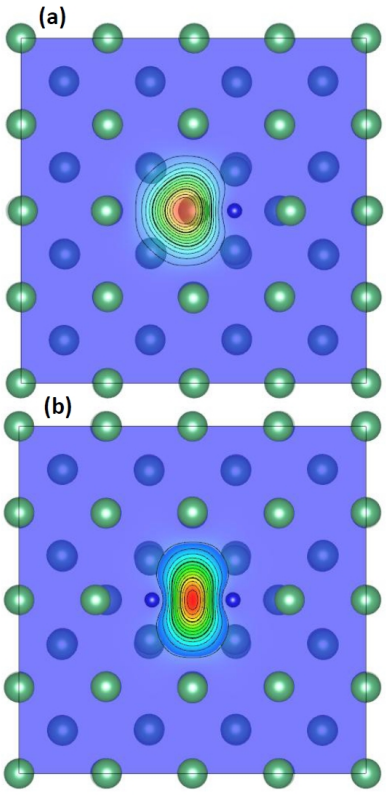

FIG. 17. Relaxed geometry of lattice ions and the positron density in the (001) plane for (a) a v-N complex, (b) a v-2N complex.

for $n \leq 2$. Hence, vacancies in Nb are able to trap up to two nitrogen atoms. v-nN complexes containing more than two nitrogen are unstable. The calculated positron

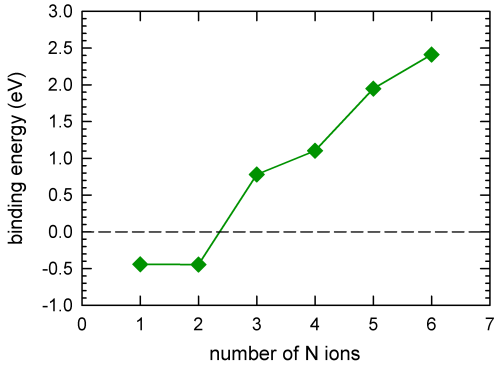

FIG. 18. Calculated binding energies of nitrogen atoms to a vacancy forming v-nN complexes.

density in the (001) plane with a v-2N complex is shown in Fig. 17b. Despite a reduction of the open volume, a v-2N complex is still able to trap positrons. However, the lifetime of positrons trapped in v-2N complexes is only 155 ps, i.e. it is significantly shortened compared to v-N.

The calculated momentum distributions of annihilating electron-positron pairs (ratio curves with respect to pure Nb) for stable v-nN complexes are plotted in Fig. 19. The presence of nitrogen bound to a vacancy leads to a peak located at momentum $p_L \approx 20 \times 10^{-3} m_0 c$ due to the contribution of positrons annihilated by nitrogen p electrons. For v-2N complexes, the peak at $p_L \approx 20 \times 10^{-3} m_0 c$ becomes more pronounced due to an increasing contribution of positrons annihilated in the vicinity of nitrogen.

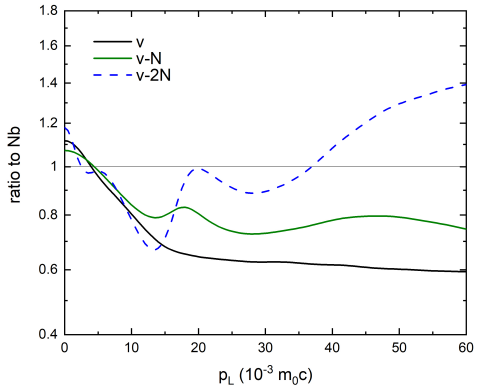

FIG. 19. Calculated momentum distributions for positrons trapped in a bare vacancy (v) and stable complexes of vacancy associated with nitrogen (v-N, v-2N). Momentum distributions are presented as ratio curves with respect to pure Nb.

4. Oxygen in Nb

Similarly to nitrogen, also oxygen absorbed in the Nb lattice is located in the octahedral interstitial site. The relaxation of Nb ions surrounding an oxygen interstitial (O_i) is similar to the case of N_i, see Fig. 16. The two nearest neighbors of O_i relax outward (displacement 0.40 Å) while the four next nearest neighbours are displaced toward O_i (displacement -0.06 Å). The formation energy of (O_i) of -4.15 eV was calculated using Eq. (C8), only replacing nitrogen by oxygen. Hence, similarly to hydrogen and nitrogen also the absorption of oxygen in the Nb lattice is an exothermic process. There is an attractive interaction between O_i and vacancies. The lowest energy configuration of a vacancy associated with oxygen (v-O) is similar to a v-N complex, i.e. the oxygen is located on the line between the vacancy and the nearest neighbour octahedral site. The oxygen is displaced 0.13 Å from the octahedral interstitial site towards the vacancy and hence, the distance of the oxygen from the vacancy is 1.53 Å. The binding energy of oxygen to a vacancy can be calculated using Eq. (C9) only replacing nitrogen by oxygen. The calculated binding energy of -0.83 eV indicates that oxygen is bound to a vacancy

significantly stronger than nitrogen. In the presence of absorbed oxygen in the Nb lattice, the vacancy formation energy is reduced to $2.79-0.83 = 1.96$ eV. The calculated

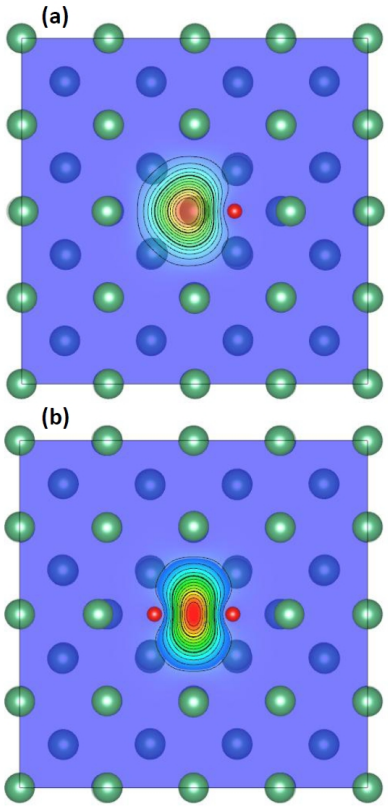

FIG. 20. Relaxed geometry of lattice ions and the positron density in the (001) plane for (a) a v-O complex, (b) a v-2O complex.

positron density in the (001) plane containing a v-O complex is plotted in Fig. 20a. Similarly to v-N, a positron can also be localized in v-O complex and the lifetime of positrons trapped in v-O were further shortened down to 188 ps.

Trapping of multiple oxygen atoms to a vacancy has been examined. The binding energy of an additional oxygen atom to a vacancy associated already with n oxygen atoms resulting in the transformation of a v-nO to a v-$(n+1)$O complex was calculated using Eq. (C10), only replacing nitrogen by oxygen and is plotted in Fig. 21 as a function of number of oxygen atoms trapped at a vacancy. Similarly to the case of nitrogen, vacancies are able to trap up to two oxygen atoms. For higher number of oxygen atoms, the v-nO complex becomes unstable.

The positron density in the (001) plane containing a v-2O complex shown in Fig. 20 is very similar to that for v-2N. The calculated lifetime of positrons trapped in v-2O is 166 ps, which is longer than the lifetime for v-2N complexes due to a smaller inward relaxation of Nb ions surrounding the v-2O complex.

The calculated momentum distributions of annihilating electron-positron pairs (ratio curves with respect to

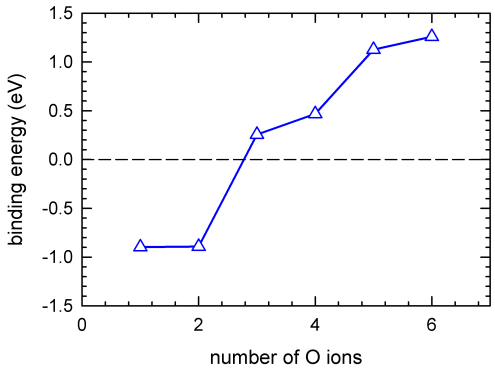

FIG. 21. Calculated binding energies of oxygen atoms to a vacancy forming v-nO complexes.

pure Nb) for stable v-nO complexes (v-O, v-2O) are plotted in Fig. 22. Similarly to the case of nitrogen, also the presence of oxygen bound to a vacancy is reflected by a peak at momentum $p_L \approx 20 \times 10^{-3} m_0 c$ due to contributions of positrons annihilated by oxygen p electrons. Since oxygen contains one more p electron, the peak for a v-O complex is more pronounced than for a v-N complex. For v-2O complex the peak further increases due to increasing contribution of positrons annihilated in the vicinity of oxygen atoms.

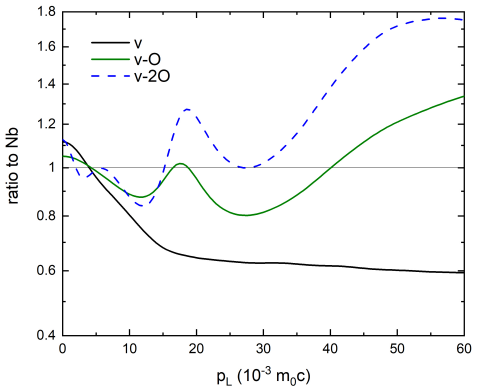

FIG. 22. Calculated momentum distributions for positrons trapped in a bare vacancy (v) and stable complexes of vacancy associated with oxygen (v-O, v-2O). Momentum distributions are presented as ratio curves with respect to pure Nb.

5. H trapping in v-N and v-O complexes

It is interesting to examine the possibility of hydrogen trapping in vacancies containing already trapped O or N atoms leading to the formation of v-N-nH or v-O-nH complexes. It was found that in the lowest energy con-

figuration of such complexes, hydrogen atoms are now located close to the octahedral interstitial sites around a vacancy which are not occupied by an oxygen or nitrogen interstitial. As an example, Fig. 23 shows the equilibrium configuration of v-N-5H complex. The binding energy of

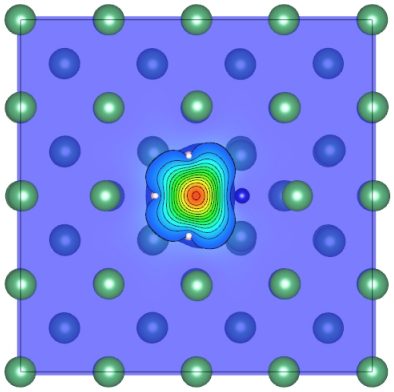

FIG. 23. Relaxed ion positions and the positron density in the (001) plane containing a v-N-5H complex.

a hydrogen atom to a vacancy associated already with a nitrogen atom and n hydrogen atoms leading to a transformation of a v-N-nH complex to a v-N-(n+1)H complex can be calculated from the expression

$$\begin{aligned} E_{B,\text{v-N-}(n+1)\text{N}} = \; & E[N-1, \text{v-N-}(n+1)\text{H}] + E[N, \text{bulk}] + ZPE[\text{v-N-}(n+1)\text{H}] \\ & - \left(E[N-1, \text{v-N-}n\text{H}] + E[N, \text{H}_i] + ZPE[\text{v-N-}n\text{H}] + ZPE[\text{H}_i]\right), \end{aligned}$$

where $E[N-1, \text{v-N-}(n+1)\text{H}]$ and $E[N-1, \text{v-N-}n\text{H}]$ denote the energy of a supercell containing v-N-($n+1$)H and v-N-nH complexes, respectively. The binding energy of an additional hydrogen atom to a v-O-nH complex can be calculated using the same equation only replacing nitrogen by oxygen. The calculated binding energies are plotted in Fig. 12 as a function of the number of hydrogen atoms. From an inspection of the figure one can conclude that both v-N and v-O complexes are able to trap up to 5 hydrogen atoms. The strength of the hydrogen bond to a v-N and v-O complex is comparable but weaker than for a bare vacancy. The absolute values of the binding energy of additional hydrogen atoms decreases with an increasing number of hydrogen atoms associated with v-N or v-O complexes, indicating that binding of additional hydrogen atoms to the complex becomes weaker and weaker. The lifetimes of positrons trapped in v-N-nH and v-O-nH complexes are plotted in Fig. 14 as a function of the number n of hydrogen atoms. Positron lifetimes for v-N-nH and v-O-nH complexes are very similar and monotonically decreases towards the bulk lifetime with increasing number of H atoms.